Copyright Undertaking

This thesis is protected by copyright, with all rights reserved.

By reading and using the thesis, the reader understands and agrees to the following terms:

1. The reader will abide by the rules and legal ordinances governing copyright regarding the use of the thesis.

2. The reader will use the thesis for the purpose of research or private study only and not for distribution or further reproduction or any other purpose.

3. The reader agrees to indemnify and hold the University harmless from and against any loss, damage, cost, liability or expenses arising from copyright infringement or unauthorized usage.

THE HONG KONG POLYTECHNIC UNIVERSITY

THE DEPARTMENT OF APPLIED PHYSICS

DEVELOPMENT OF LEAD-FREE PIEZOELECTRIC CERAMIC RESONATORS FOR HIGH-FREQUENCY OSCILLATOR APPLICATIONS

WONG HO YAN

A THESIS SUBMITTED IN PARTIAL FULFILMENT OF THE REQUIREMENTS FOR THE DEGREE OF MASTER OF PHILOSOPHY

October, 2008

CERTIFICATE OF ORIGINALITY

I hereby declare that this thesis is my own work and that, to the best of my knowledge and belief, it reproduces no material previously published or written, nor material that has been accepted for the award of any other degree or diploma, except where due acknowledgement has been made in the text.

(Signed)

___WONG HO YAN___ (Name of Student)

Abstract

The main objective of the present work is to develop lead-free piezoelectric ceramic resonators for high-frequency oscillator applications. Lead-free piezoelectric ceramics have been extensively studied recently for replacing the widely used lead-based piezoelectric materials for environmental protection reasons. $CaBi_4Ti_4O_{15}$ (CBT) is one of the most important lead-free piezoelectric ceramics. It has a very high Curie temperature T_C (790 °C), a high resistivity ($10^{12} \Omega \cdot cm$) and a low dielectric loss *tanδ* (0.2 %). Hence it has been widely studied for high-temperature and high-frequency applications. Recently, CeO-modified $[(Na_{0.5}K_{0.5})_{0.94}Li_{0.06}]_{0.5}Bi_{4.5}Ti_4O_{15}$ (MBT) has been developed. The piezoelectric properties of the ceramic have been improved significantly, giving a large increase in the piezoelectric coefficient d_{33} (28 vs 18 pC/N). In the present work, CuO and a complex of Cu/Ba (in a molar ratio 71.5/28.5) have been used to further improve the physical properties of the CBT and MBT ceramics for the high-frequency resonator applications.

Our results show that the doping of CuO is effective in improving the densification, enhancing the piezoelectric properties and reducing the dielectric loss tanδ. For the CBT ceramic doped with 0.3 wt% CuO, the density increases from 6660 to 6942 kg/m^3, d_{33} increases from 10.1 to 12.4 pC/N, and *tanδ* decreases from 0.27 to 0.12 %. On the other hand, the Cu/Ba complex is effective in decreasing the sintering temperature of the CBT and MBT ceramics. The Cu/Ba complex becomes molten at a eutectic temperature of 890°C. As a result, because of the liquid-phase

which promoting the densification, the ceramics can be well-sintered at a lower temperature. For the CBT ceramic added with 0.30 wt% of the Cu/Ba complex (CBT-Cu/Ba-0.30), the sintering temperature is decreased from 1200 °C to 990 $^{\circ}$C, while the other physical properties are remained almost unchanged or even improved slightly. It has a high ρ (6756 kg/m^3), a large d_{33} (11.6 pC/N), a large planar-mode electromechanical coupling coefficient (k_p = 3.6 %) and a high resistivity (ρ_r = 2.4×10^{13} Ω·cm). Unlike CBT, there is degradation in the piezoelectric and dielectric properties of the MBT ceramics, even at a very low addition level of Cu/Ba. Nevertheless, besides the low sintering temperature (1000°C), the MBT ceramic added with 0.4 wt% Cu/Ba (MBT-Cu/Ba-0.40) has a relatively large d_{33} (24.5 pC/N) and a high ρ_r (2.9×10^{13} Ω·cm).

Because of the good piezoelectric properties and low sintering temperature, CBT-Cu/Ba-0.30 and MBT-Cu/Ba-0.40 have been used to fabricate high-frequency double-layered ceramic resonators. The resonator has a pair of top and bottom electrodes and an inner electrode in between them; all of them are of the same dimensions (2 mm and 3 mm in diameter) and smaller than the lateral dimension of the resonator (~5.4mm × 4.5 mm). As the sintering temperature for CBT-Cu/Ba-0.30 and MBT-Cu/Ba-0.40 are below 1000°C, Ag70/Pd30 inner electrode, instead of Pt, can be used for cofiring with the ceramics, and hence there is a great saving in the production cost. Our results reveal that the spurious vibrations of the resonators have been successfully suppressed. This should be party due to the smaller electrodes which is one of the typical approaches in the energy trapping technique to confine the vibrations in the electroded region and hence to

reduce the standing waves formed by the reflected waves from the sample edge. This should also partly due to the second harmonic thickness extension mode vibrations. Our results also reveal that although the MBT-Cu/Ba-0.4 ceramic has better piezoelectric properties, its performance as a resonator is not as good as CBT-Cu/Ba-0.30. For the CBT-Cu/Ba-0.30 double-layered resonator, it has a relatively "clean" resonance response and a lower temperature coefficient of frequency (*TCF* =-39.3 ppm/°C). It also has a relatively low impedance at resonance (14 and 30 Ω for 3-mm and 2-mm electrodes, respectively), which is very close to the value for a commercially available PZT resonator. These suggest that the CBT-Cu/Ba-0.30 lead-free double-layered resonators have good potential to replace the lead-based resonators.

Acknowledgments

I would like to express my appreciation to my supervisors Dr. K. W. Kwok and for his excellent guidance and constant encouragement throughout the whole period of my research work. I would also like to thank Mr. W. O. Chu from Hong Kong X'tals Ltd. for his helpful discussions about the resonance responses of ceramic resonator.

I gratefully acknowledge the financial support from the Innovation and Technology Fund of the HKSAR Government and Hong Kong X'tals Ltd., and technical support provided by the Centre for Smart Materials of the Hong Kong Polytechnic University.

The last but not least, I would like to thank my parents for their understanding, constant support and encouragement.

Table of Contents

List of Figures

List of Tables

Chapter One

Introduction

1.1 Background

There are many types of oscillators, and many different circuit configurations that produce oscillations. Some oscillators produce sinusoidal signal, and others produce nonsinusoidal signal. Nonsinusoidal oscillators, such as pulse and ramp (or sawtooth) oscillators, find use in timing and control applications. Pulse oscillators are commonly found in digital-system clocks, and ramp oscillators are found in the horizontal sweep circuit of oscilloscopes and television sets. Sinusoidal oscillators are used in many applications, for example, in consumer electronic equipment (such as radios, TVs, and VCRs), in test equipment (such as network analyzers and signal generators), and in wireless systems.

Oscillators can have frequency variations, which can be classified as long term and short term. Long-term frequency stability is the ability of the oscillator to maintain the frequency of oscillation that does not depend on changes in temperature, aging of components (such as resonators), and so on. Those frequency variations that occur over a long period of time result from changes in the components that directly affect the frequency of oscillation ω_o. The long-term stability of an oscillator is predictable and is commonly expressed as a frequency drift. Short-term stability describes the oscillator's frequency variation over a short

period of time. Short-term frequency variations are usually produced by noise and mechanical vibrations. For example, the properties of the resonator are functions of mechanical vibrations. An external mechanical vibration can introduce a change in the oscillation frequency of the resonator.

1.1.1 Quartz Resonators

Crystal-controlled oscillators use a crystal usually made from quartz crystal for their operations. Quartz exhibits a property: when a mechanical stress is applied to the crystal along a certain direction or axis, a voltage is generated. Conversely, if an ac voltage is applied to the crystal, it will change its physical shape, producing mechanical vibrations. These phenomena between the mechanical and electrical effects are called the direct and converse piezoelectric effect, respectively. There are also other crystalline materials exhibiting the piezoelectric effects, but quartz is the most suitable material for the oscillators. If the frequency of the applied signal is equal to the mechanical resonance frequency of the quartz, it will vibrate significantly and only a small voltage is required to keep it vibrating. In fact, the main reason for using a quartz oscillator instead of an LC tuned oscillator is that the mechanical quality factor Q associated with the quartz oscillator is usually 1000 to 10000 times greater than those associated with the LC tuned oscillators.

The quartz will act like a very high Q tuned circuit, permitting oscillations only at its resonance frequency. At frequencies slightly above and below its resonance frequency, the amplitude of the crystal vibration becomes essentially zero.

The oscillation frequency of a quartz oscillator is the same at the resonance frequency of the quartz.

(a)   (b)
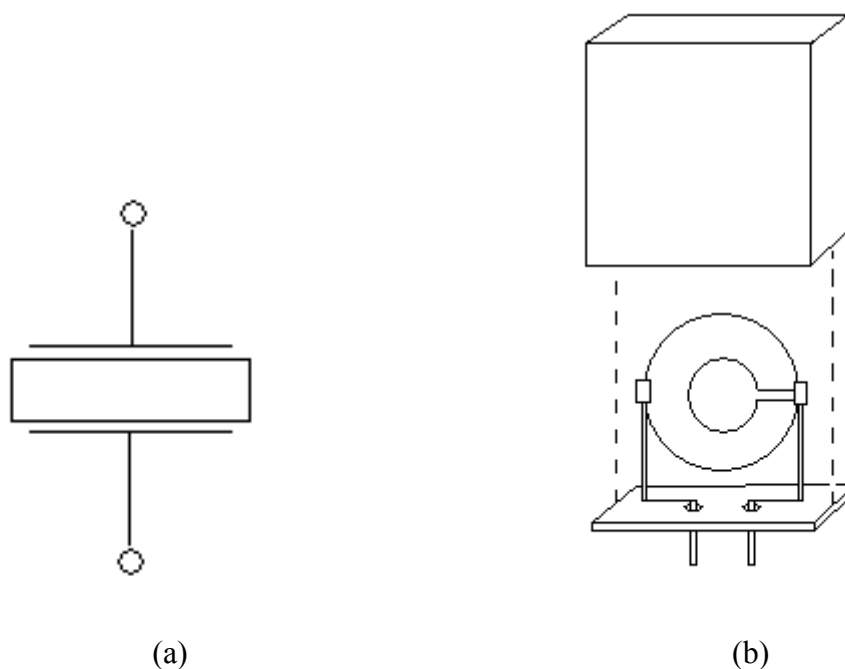
Figure 1.1   (a) Schematic symbol for a quartz resonator, (b) Schematic diagram for a commercially available quartz resonator.

The schematic symbol for a quartz resonator is shown in Figure 1.1(a), while the schematic diagram for a typical commercially available quartz resonator with mountings is shown in Figure 1.1(b). As shown in Figure 1.1(b), the quartz crystal plate is supported by springs or wires attached to points that do not attenuate the mechanical vibrations. The wires are then connected to the pins for external electrical connections. The impedance spectrum of a quartz resonator is shown in Figure 1.2 [1].
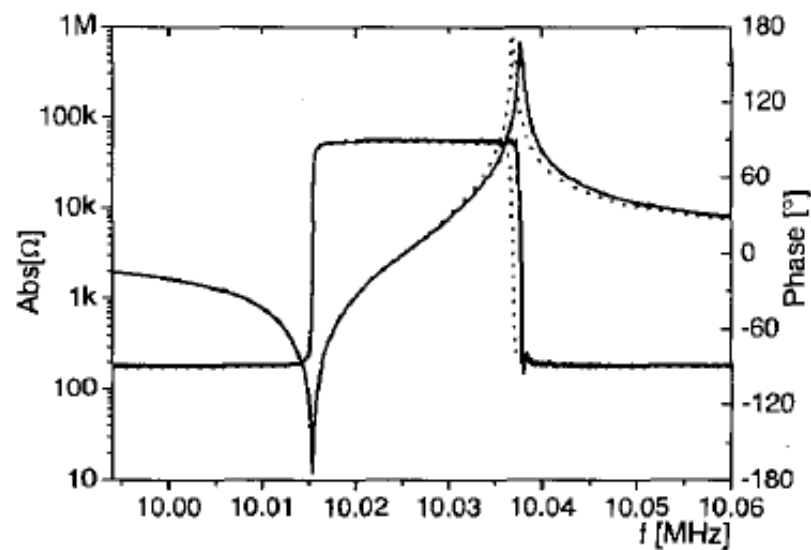
Figure 1.2   Impedance spectrum of a quartz crystal resonator. [1]

The quartz plates used in oscillators must be cut and polished to extremely accurate dimensions. Quartz is classified according to the manner in which it was cut from the original crystal. A variety of cuts are used, among them are the X-, Y-, AT-, BT-, GT-, and SC-cuts. Quartz plates prepared from different cuts exhibit different characteristics, especially the temperature dependence. The X-cut quartz has a negative temperature coefficient. That is, the resonance frequency decreases with increasing temperature. The Y-cut quartz has a positive temperature coefficient. Temperature stability in quartz refers to the variation of its resonance frequency with temperature. It is defined as the frequency drift in ppm (part per million) over a specified temperature range. Typical requirement for the temperature stability is from 10 to 100 ppm in hertz per degrees Celsius. The AT-cut quartz is very popular because of its small temperature variation. For example, the temperature stability of an AT-cut quartz can be as small as 30 ppm/°C over a temperature range from -55°C

to 105°C. Frequency tolerance, also expressed in ppm, describes the deviation of the actual resonator frequency as compared to the specified frequency at a reference temperature (such as 25°C). For example, a 3.24500 MHz crystal with a frequency tolerance of 10 ppm is fabricated inaccurately from one with a specified frequency of 3.24555 MHz.

The sum of the frequency tolerance and temperature stability is known as the overall tolerance. The overall tolerance is a measure of the frequency deviation over a temperature range of operation with respect to the nominal frequency.

1.1.2   Ceramic Resonators

Ceramic resonators (CRs) make use of the mechanical resonances that occur in piezoelectric ceramics (usually lead zirconium titanate PZT). In general, the performance of ceramic resonators is better than that of *LC* tuned oscillators, but poorer than that of quartz resonators. For example, quartz resonators have a typical temperature coefficient of 10^{-6}/°C, but that of CRs is about 10^{-5}/°C. However, CRs are smaller in size and less expensive than crystal resonators. Figure 1.3 shows the typical commercially available CRs with two and three leads. CRs with three leads contain an internal built-in load capacitor. Similar to quartz resonators, CRs are widely used in digital-clock applications [2].

(a)   (b)
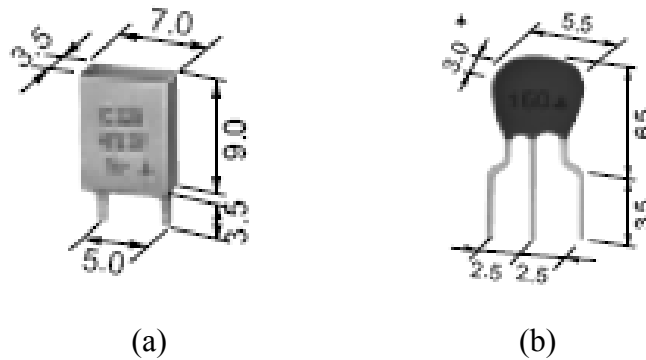
Figure 1.3   Typical commercially available CRs (a) with two leads, (b) with three leads. [2]

As shown in Figure 1.4 (a), the schematic symbol and equivalent circuit of the CRs are identical to those of the quartz resonators. The impedance spectrum of a PZT resonator (Figure 1.5) is similar to that of a crystal resonator as shown in Figure 1.2. Between the series (f_s) and parallel (f_a) resonances, the resonator is inductive. The equivalent electrical circuit of a piezoelectrics vibrator is shown in Figure 1.4(b).

(a)   (b)
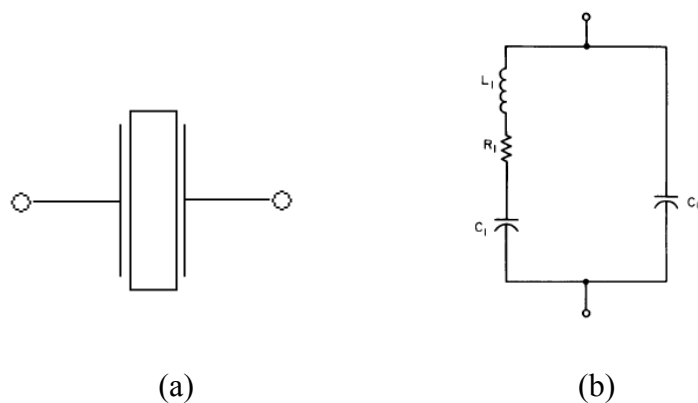
Figure 1.4   (a) CR symbol, (b) equivalent circuit of a piezoelectric vibrator.
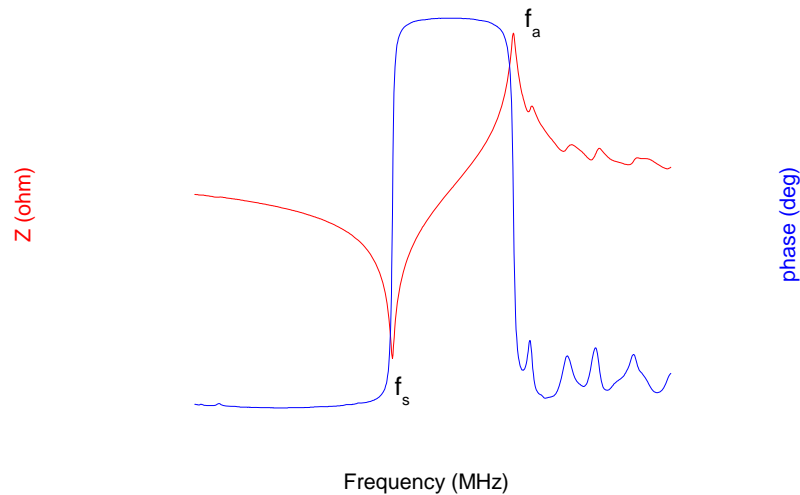
Figure 1.5   Impedance spectrum of PZT resonator.

1.2   Materials for Resonators

1.2.1   Piezoelectricity

The direct piezoelectric effect was discovered by Pierre and Paul-Jacques Curie in 1880. They found that when certain types of crystals were compressed along certain axes, charges were induced on the surface of the crystals [3]. The piezoelectric behavior of such a crystal can be elucidated in Figure 1.6. Later on, it was also found that those crystals could be deformed by the application of an electric field along certain axes. The corresponding effect is called the converse piezoelectric effect.
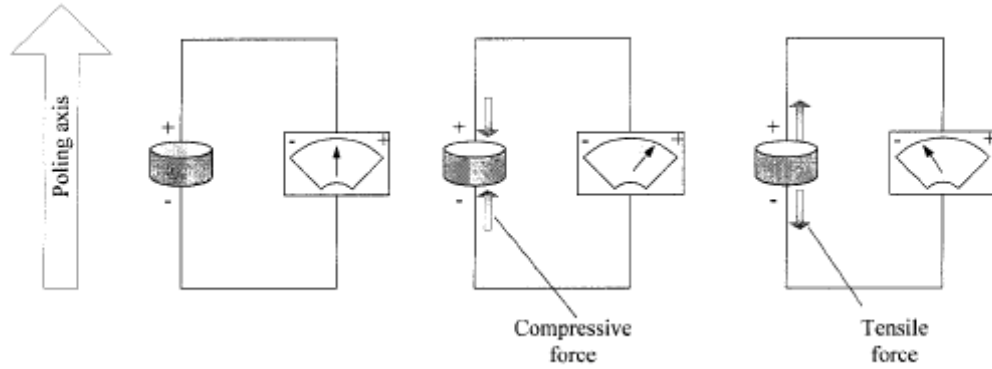
Figure 1.6   (Direct) piezoelectric behavior of a piezoelectric crystal.

The following equations (1.1) and (1.2) can be used to describe the electrical and mechanical variables in linear piezoelectric theory:

$$S_{ij} = s_{ijkl} X_{kl} + d_{mij} E_m \qquad (1.1)$$

$$D_{ij} = d_{ikl} X_{kl} + \varepsilon_o \varepsilon_{r_{ij}} E_j \qquad (1.2)$$

where S is the strain, s is the elastic compliance, X is the elastic stress, d is the piezoelectric coefficient, E is the electric field, D is the dielectric displacement, ε_o is the permittivity of free space and ε_r is the relative permittivity of the material. Equation 1.1 describes the converse piezoelectric effect and Equation 1.2 describes the direct piezoelectric effect [4].

The piezoelectric effects are due to the asymmetry of the crystal structure. Most of technically important and widely used piezoelectric ceramics have the perovskite (ABO_3) crystal structure as shown in Figure 1.7.
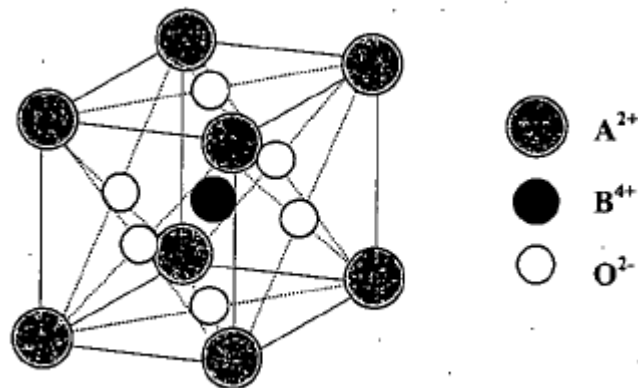
Figure 1.7   Perovskite ABO$_3$ crystal structure.

Perovskite ABO$_3$ structure is constructed by the superimposition of three sets of simple cubic structure of A, B, and O atoms. Since the larger atom A increases the overall size of the ABO$_3$ structure, the smaller atom B can occupy the minimum energy position which is off-centered from the original octahedron cage, and thus forming an electric dipole. The atom B changes its position, and accordingly the electric dipole switches, with the applied electric field.

Because of the random orientation of the domains (region with uniformly aligned dipoles), as-prepared piezoelectric materials do not exhibit any piezoelectric effect. The materials are isotropic. A large external electric field has to be applied across the piezoelectric material to align the dipoles in order to induce the piezoelectricity of the material. This process is called poling, and the poled materials become polarized and anisotropic.

1.2.2   Ferroelectricity

The relationship between piezoelectrics and ferroelectrics is shown in Figure 1.8. It shows that all the ferroelectrics are piezoelectric while part of the piezoelectrics are ferroelectric. [3]
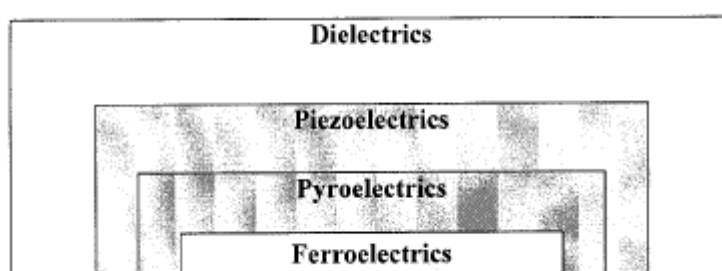
Figure 1.8   The relationships of dielectrics, piezoelectrics, pyroelectrics, and ferroelectrics.

A ferroelectric material has a spontaneous polarization, which can be reversed by the application of a strong electric field [6]. Polarization is the dipole moment density and has a unit of coulomb per meter square (C/m^2). One of the important features of ferroelectric materials is the polarization hysteresis, which is caused by the lag of the polarization switching from the applying field and is generally manifested by a polarization hysteresis (P-E) loop as shown in Figure 1.9.
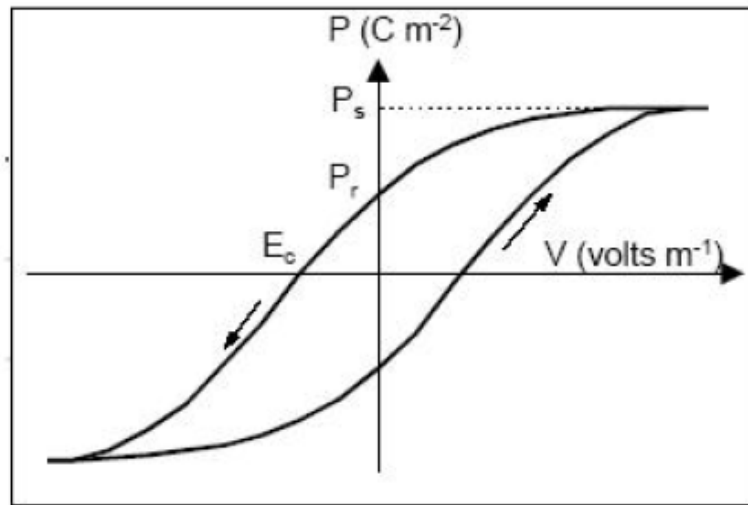
Figure 1.9   A typical P-E hysteresis loop of a ferroelectric material [5].

When a sufficiently high electric field is applied to a ferroelectric material, the electric dipoles will be aligned and hence the (net) polarization will increase, reaching a maximum value known as the saturation polarization P_s. After the removal of the electric field, a polarization is remained in the material, which is called the remanent polarization P_r. The coercive field E_c is the electric field (in opposite direction) required to reduce the polarization to zero.

The remanent polarization can be removed by thermal energy. A ferroelectric material will undergo a ferroelectric-paraelectric phase transition at a temperature called Cuire temperature T_c. Above T_c, the material is transformed to the paraelectric phase and the spontaneous polarization of the material decreases to zero, hence exhibiting no ferroelectricity. As the temperature decrease below T_c, the material is transformed back to the ferroelectric phase, but with zero (net) polarization. The orientation of the domains becomes completely random after the transition from high temperatures.

1.2.3   Quartz

A quartz resonator is a piece of piezoelectric material precisely dimensioned and oriented with respect to the crystallographic axes of the material and equipped with one or more pairs of conducting electrodes. Many different substances have been investigated as possible candidates for piezoelectric resonators, but for many years, quartz resonators have been preferred in satisfying needs for precise frequency control and selection. Compared to other resonators, for example piezoelectric resonators based on ceramics or other single crystals, the quartz resonator has a unique combination of properties. The material properties of quartz are extremely stable and highly repeatable from one specimen to another. The acoustic loss of quartz is particularly low, leading directly to one of the key properties of the quartz resonators, the extremely high mechanical quailty factor Q_m (or *Q factor)*. The Q_m of mounted quartz resonators typically range from tens of thousands to several hundreds of thousands, orders of magnitude better than the best LC circuits.

The Q_m of a resonance is defined as [7]

$$Q = 2\pi \frac{Energy \quad stored \quad per \quad cycle}{Energy \quad dissipated \quad per \quad cycle} \tag{1.3}$$

The unique ability for quartz resonators to control the resonance frequency is its high Q_m and low electromechanical coupling coefficient *k.* The electromechanical coupling coefficient *k* is defined as

$$k = \sqrt{\frac{Energy \quad stored \quad elastically}{Energy \quad stored \quad electrically}} \qquad (1.4)$$

The value of k^2 for the AT-cut quartz is less than 1 percent. This means that the electric driving system is very loosely coupled to the mechanical system and thus the former has very little influence over the latter. Nevertheless, because of the high Q_m, even such a small effect is sufficient to excite and maintain vibrations in the quartz resonator, which is what makes it an effective transducer for controlling a frequency.

The second key property of quartz resonators is the thermal stability. Quartz crystal can be cut into quartz plates (or quartz blanks) with different shapes, orientations and hence different vibration modes. It is hence possible to control the frequency-temperature characteristics of the resonator to within close limits by an appropriate choice. The most commonly used type of quartz resonators use the AT-cut quartz plate which has a frequency-temperature stability over a reasonably wide temperature range required by modern communication systems [8]. The thermal stability of a resonator is quantified by the temperature coefficient of frequency *TCF* which is define as

$$TCF = \frac{f_{r[80^o C]} - f_{r[-20^o C]}}{f_{r[20^o C]} \times 100^o C} \qquad (1.5)$$

1.2.4   Piezoelectric Ceramics

For ceramic resonators, most of them are made of lead-based piezoelectric materials, such as lead zirconate titanate (PZT) [9-10]. As lead has an adverse impact on the global environment and the human body, various countries such as German and Japan have scheduled to phase out lead-containing products. In order to cope with the change, it is of great importance and need to carry out research work on developing lead-free piezoelectric materials and exploring the use of them in fabricating resonators for replacing the conventional lead-based products.

Of the lead-free piezoelectric ceramic materials, bismuth layer-structured ferroelectric (BLSF) materials are the most suited to oscillator applications. Because of the high Q_m and low k, they are suitable for high rate data transfer systems where fine frequency tolerances are essential. In addition, they also have a high Curie temperature T_c, which is another advantage of materials for resonator applications [11-17].

Table 1.1 compares the dielectric and piezoelectric properties of various kinds of piezoelectric ceramics, while Table 1.2 summarizes the properties of a number of BLSFs which have been recently studied for resonator applications. The variations of the relative dielectric permittivity and the change in the resonance frequency for those BLSFs are shown in Figures 1.10 and 1.11, respectively [18]. As the electromechanical coupling coefficient k for $SrBi_2Nb_2O_9$ (SBN), $CaBi_4Ti_4O_{15}$ (CBT), $SrBi_4Ti_4O_{15}$ (SBTi), and $Na_{0.5}Bi_4Ti_4O_{15}$ (NBT) is about 15 % and 20 %, and

their mechanical quality factor Q_m is higher than 2000. These suggest that they are ideal for practical resonator applications.

Table 1.1 Dielectric and piezoelectric properties of some typical piezoelectric ceramic materials. [18]

Material family	Main composition	ε_r	k (%)	Q_m	TCF (ppm/^{o}C)	Tc (^{o}C)
Alkaline niobate	$(Li,Na)NbO_3$ $(Li,Na)NbO_3$ $(K,Na)NbO_3$	120 90 1000	46 (TE1) 30 (TE1) 35 (TE1)	300 2000 100	-100 -120 -280	450 400 320
Bismuth layer-structured ferroelectrics	$SrBi_2Nb_2O_9$ $CaBi_4Ti_4O_{15}$	130 130	17 (TE2) 14 (TE2)	2200 3000	-10 -30	~400 790
Tungsten bronze	$(Ba,Sr)_2NaNb_5O_{15}$	500	18 (TE1)	400	+15	260
Bismuth titanate	$(Bi,Na)TiO_3$	800	42 (TE1)	40	-360	180
Oriented zinc oxides	ZnO	10	25 (radial)	26000	-40	None
PZT (for resonators)	$Pb(Ti,Zr)O_3$	500-1500	30-50 (TS1)	1000-3000	-20 to +20	300-350
Lead titanate	$PbTiO_3$	150-250	~10 (TE3) ~30 (TE2)	2000-3000	-20 to +20	300-400

Table 1.2   Dielectric and piezoelectric properties of various BLSF materials. [18]

BLSFs	$\varepsilon^{T}_{33}/\varepsilon_{o}$	k_t (%)	Q_m	TCF (ppm/^{o}C) (-20 ^{o}C to 80 ^{o}C)	T_c (^{o}C)
SrBi$_2$Nb$_2$O$_9$ (SBN)	130	17	2200	-20	420
CaBi$_4$Ti$_4$O$_{15}$ (CBT)	150	15	3000	-30	810
SrBi$_4$Ti$_4$O$_{15}$ (SBTi)	130	20	5000	-50	520
Na$_{0.5}$Bi$_4$Ti$_4$O$_{15}$ (NBT)	120	25	2000	-150	650
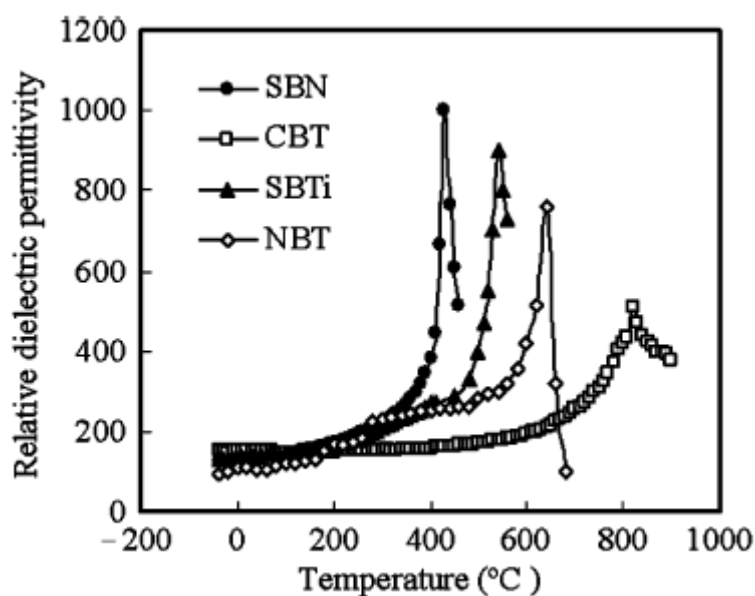
Figure 1.10   Variation of the relative dielectric permittivity with temperature for various BLSFs (measured at 1MHz). [18]
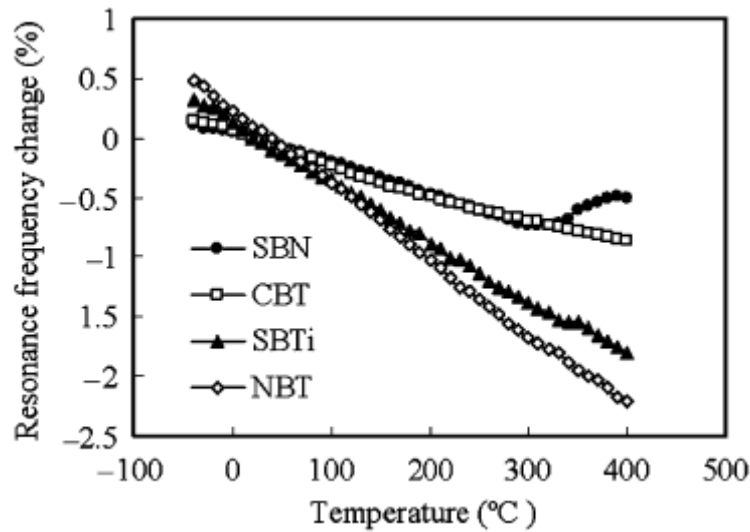
Figure 1.11   Variation of the change in the resonance frequency with temperature for various BLSFs. The resonance frequency was measured for the TE1 mode vibration of the single ceramic plates. [18]
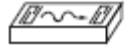
1.3   Energy Trapping

The most essential characteristic of a resonator is the capability of having a "clean" single-mode resonance. As shown in Table 1.3, for the low-frequency vibration modes, such as flexural mode and radial mode, the resonance frequency is in the range of hundred kHz [2]. As the vibration frequency is low, they are usually the first resonance among all vibration modes. Accordingly, they will not be coupled or affected, hence exhibiting a "clean" single-mode vibration. However, resonators for clock generators in the applications of high speed data transfer, resonance frequency is in the range from several MHz to several ten MHz. To achieve such a high resonance frequency, the resonance mode is usually the thickness extension (TE) mode. However, when the resonator is excited at the

thickness extension mode, other vibration modes, such as surface Lamb waves, will usually be excited, forming the so-called spurious vibrations. The spurious vibrations in the vicinity of the desired resonance frequency will affect the performance of the resonator significantly.

Table 1.3   Vibration mode and frequency range. [2]

Vibration Mode / Frequency (Hz)		1k	10k	100k	1M	10M	100M	1G
1 Flexural mode		████						
2 Length mode				███				
3 Area expansion mode					███			
4 Radius vibration					███			
5 Shear thickness mode						██		
6 Thickness expander mode						████		
7 Surface acoustic wave							████	

[Note] : ←——→ show the direction of vibration

The energy trapping technique is usually applied in the commercial resonators to suppress the spurious vibrations. The concept of the energy trapping was first introduced by Mortley in 1946 in his paper "A waveguide theory of piezoelectric resonance" [19]. Shockley et al. called this phenomenon energy trapping and performed a theoretical analysis of this phenomenon independently [20-21]. The theory of energy trapping by these authors was devised to explain Guttwein's

observation that excessive electrode thickness introduced spurious modes [22].

Figure 1.12 Schematic diagram of an "energy-trapped" resonator.

The energy trapping technique applies a pair of partial electrodes as shown in Figure 1.12. Owing to the mass loading effect, the cutoff frequency for the electroded and unelectroded regions, ω_e and ω_s, respectively, are different, with $\omega_e < \omega_s$. For a resonator, the cutoff frequency is the resonance frequency of the desired vibration mode. Below the cutoff frequency, no acoustic wave can propagate. Accordingly, the acoustic waves with frequencies between ω_e and ω_s, i.e. the spurious vibrations, can propagate freely only in the electroded region but not in the unelectroded region. In the unelectroded region, the vibration energy tails off exponentially with distance away from the electrodes. This exponential decay is not associated with energy loss but acts to trap the vibration energy under the electrodes only. As the spurious vibrations cannot propagate in the unelectoded region, corresponding standing waves cannot occur. As a result, the spurious vibrations are suppressed, or shifted to a higher frequency. It has been shown that for the Poisson ratio of the material has to be larger than 1/3 for the fundamental thickness extension mode (TE1), while it can be smaller than 0.40 for the TE3 mode. For most of the lead-based piezoelectric ceramics, their Poisson ratio is less than 0.40, so the energy trapping technique can only be applied for the ceramic resonator

operating at the TE3 mode. However, for those resonators, there are additional spurious vibrations arisen from the TE1 mode.

TE2-mode resonator can be fabricated by applying a pair of partial outer electrodes and a buried inner electrode as shown in Figure 1.13. It has been shown that energy trapping can be realized in such resonators even for the piezoelectric material with a Poisson ratio less than 1/3. This can be explained by the dispersion characteristics.
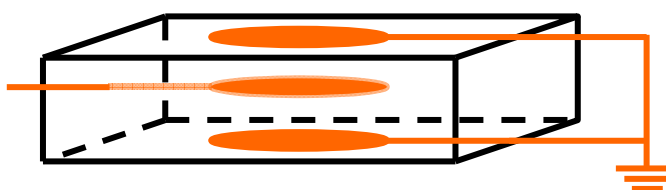
Figure 1.13   Schematic diagram of a TE2-mode resonator.

The dispersion curve plots the relationship between the frequency and wave number. Dispersion curves for the TE1 mode and TE2 mode of $PbTiO_3$ material are shown in Figure 1.14. There are two cutoff frequencies, one is for the mode under the electrode region and another is for the mode outside the electrode region. Due to the loading effect, the cutoff frequency under the electrode region is lower than the one outside the electrode region. The real wave number means that the wave can propagate while the imaginary wave number means the damping of vibration. The wave cannot propagate outside the electrode region. This means that the vibration is concentrated under the electrode region.
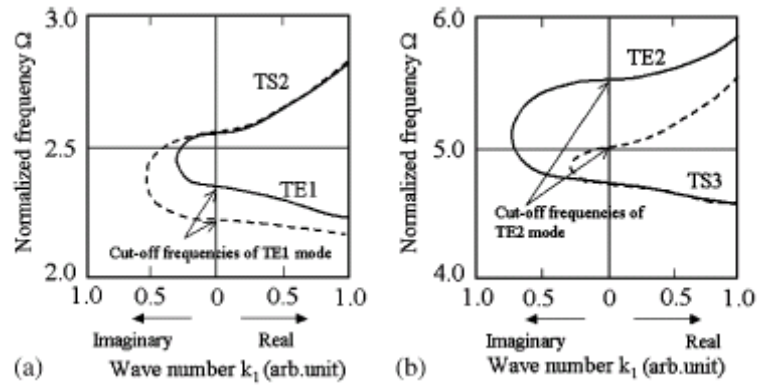
Figure 1.14   Dispersion curves for the TE mode vibrations; (a) TE1 mode, (b) TE2 mode. Normalized frequency Ω is defined as $\dfrac{\omega h}{\sqrt{c_{44}^{E}/\rho}}$, where h is a half the thickness of the plate. Solid and broken lines represent the characteristics outside the electrode region and under the electrode region, repsectively. [18]

However, as shown in Figure 1.14(a), the odd-number harmonic of the TE mode, such as TE1 and TE3, it will connect to the even harmonic of thickness shear (TS) mode since they are both symmetrical. As the Poisson ratio of piezoelectric ceramics is usually less than 1/3, the cutoff frequency of the TE1 mode is lower than that of the TS2 mode and they are close to each other. The frequency decreases with increasing the wave number for the TE1 mode. This means that waves can propagate outside the electrode region and reflect back, thus forming standing waves. As a result, waves will superpose and single-mode resonance cannot be obtained. Therefore, it is difficult to obtain a single-mode resonator with TE1 mode vibration.

As shown in Figure 1.14(b), the TE2 mode may couple with the TS3 mode since they are both asymmetric. However, as their cutoff frequencies are sufficiently separated and the frequency increases with increasing the wave number, single-mode resonance characteristic of the TE2 mode vibration can be obtained even for the material with a Poisson ratio less than 1/3 [18].

1.4 Scope of Work

The main objective of the present project is to develop lead-free piezoelectric ceramic resonators for high-frequency oscillator applications (~ 20 MHz). Due to their low k and high Q_m, Bismuth layer-structured ferroelectrics (BLSFs) is chosen as based material. In order to obtain single mode resonance, energy trapping technique and double-layered structure are applied on the resonator.

In Chapter 2, the fabrication processes of bismuth layer-structured ferroelectric (BLSF) ceramics and double-layered resonators are presented.

In Chapter 3, materials characterizations of the BLSF ceramics are presented.

In chapter 4, designs and characterization of resonators are presented

In Chapter 5, the conclusions and suggestions for future work are presented.

Chapter Two

Fabrication of Ceramic Disks and

Double-layerd Resonators

2.1 Introduction

In this project, bismuth layer-structured ferroelectrics (BLSFs) were used as materials for the resonators. BLSFs were first discovered by Aurivillius [23]. BLSFs have a crystal structure $(Bi_2O_2)^{2+}(A_{m-1}B_mO_{3m+1})^{2-}$ in which pseudo-perovskite blocks are sandwiched between bismuth oxide $(Bi_2O_2)^{2+}$ layers along the c axis as shown in Figure 2.1. The pseudo-perovskite blocks have the general formula of $(A_{m-1}B_mO_{3m+1})^{2-}$, where A is monovalent, divalent, trivalent cations, or a combination of them, B is tetravalent, pentavalent, hexavalent cations, or a combination of them and m is the number of BO_6 octahedra in each perovskite block, having a value from 1 to 5. In BLSFs, ferroelectricity exists mainly along the a or b axis, which is parallel to the bismuth oxide layers. The bismuth oxide layers act as insulating paraelectric layers and affect the structural distortion and electric properties of the perovskite blocks [24].
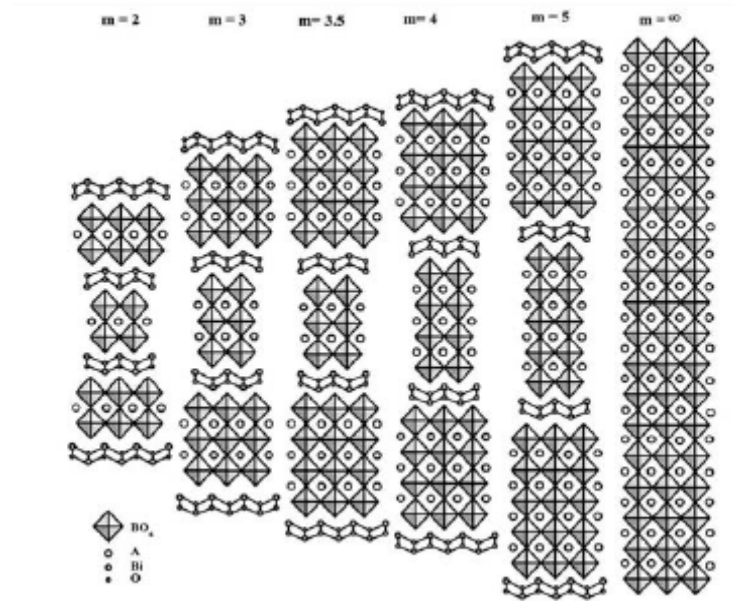
Figure 2.1   The general representation of BLSF.

$DBi_4Ti_4O_{15}$ belongs to BLSFs with $(D^{2+}_{1/3}Bi^{3+}_{2/3})$ located at the A-site of $(Bi_2O_2)^{2+}(A_{m-1}B_mO_{3m+1})^{2-}$, Ti^{4+} located at the B-site, and m = 4. D can be Ca, Ba, Sr, $(Na_{0.5}Bi_{0.5})$, $(K_{0.5}Bi_{0.5})$, or $(Li_{0.5}Bi_{0.5})$. $DBi_4Ti_4O_{15}$ and $DBi_4Ti_4O_{15}$-based piezoelectric ceramics are a series of important BLSF materials which have been widely studied for various applications in these years [25-32]. Near 40% of patents on BLSFs are for the $DBi_4Ti_4O_{15}$-base piezoelectric ceramics. The crystal structure of $DBi_4Ti_4O_{15}$ (with D = Ca) is shown in Figure 2.2.
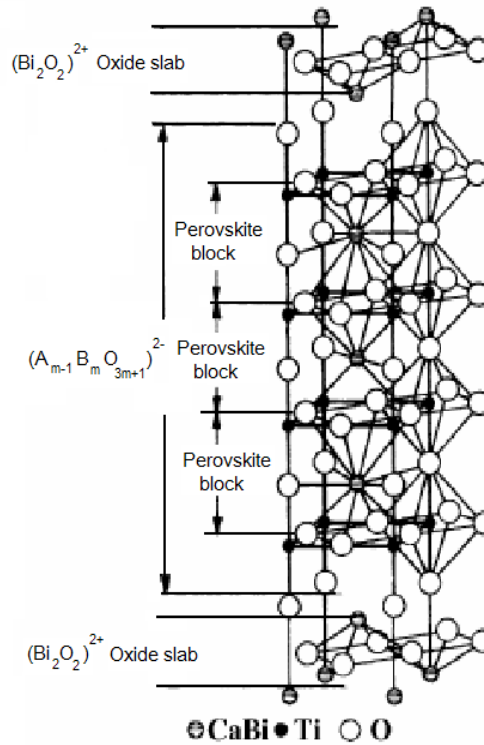
Figure 2.2   Lattice structure of $DBi_4Ti_4O_{15}$, with D = Ca.

Because of their relative high Curie temperature, low dielectric constant, strong anisotropic k_p, low dielectric loss, high Q_m, high breakdown strength, and low temperature coefficient of resonant frequency, BLSF ceramics have widely been studied recently. $CaBi_4Ti_4O_{15}$ (CBT) is a promising candidate for high temperature piezoelectric applications due to its high Curie temperature and high resistivity. The piezoelectric properties of CBT have been further improved by adding different dopants, such as SrO, Nd_2O_3, Na_2O, Li_2O, K_2O, MnO_2 [33-39]. In general, the doped CBT ceramics have larger d_{33} and smaller *tanδ*. The doping of SrO will also decrease the T_C from 790 to 520 ^{o}C, and MnO_2 will increase the Q_m. Recently, CeO_2 modified $[(Na_{0.5}K_{0.5})_{0.94}Li_{0.06}]_{0.5}Bi_{4.5}Ti_4O_{15}$ (MBT) has been developed. The piezoelectric properties of the ceramics have been significantly

improved, giving a very high d_{33} value of 28 pC/N, which is the highest value for the reported BLSF ceramics [40].

Because of the good properties, $CaBi_4Ti_4O_{15}$ (CBT) and $[(Na_{0.5}K_{0.5})_{0.94}Li_{0.06}]_{0.5}Bi_{4.5}Ti_4O_{15} + 0.5$ mol% CeO_2 (MBT) have been chosen as the base composition for this project. CuO and $BaCO_3$, will be further added to improve their properties for the resonator applications. Three compositions were prepared in this study, and their chemical formulas are listed below:

(a) $CaBi_4Ti_4O_{15} + x$ wt% CuO abbreviated as CBT-Cu-x.

(b) $CaBi_4Ti_4O_{15} + x$ wt% Cu/Ba, the molar ratio of Cu/Ba is 71.5/28.5; abbreviated as CBT-Cu/Ba-*x*.

(c) $[(Na_{0.5}K_{0.5})_{0.94}Li_{0.06}]_{0.5}Bi_{4.5}Ti_4O_{15} + 0.5$ mol% $CeO_2 + x$ wt% Cu/Ba, the molar ratio of Cu/Ba is 71.5/28.5; abbreviated as MBT-Cu/Ba-*x*.

2.2 Fabrication of CBT-based and MBT-based Ceramics

2.2.1   Mixing, Calcination, Sintering and Surface Finishing

Raw materials were evaluated on the basis of purity and particle size. Small particle size is desired for attainment of chemical equilibrium, particularly in solid state formation of solid solutions. Impurities can also affect the reactivity, as well as

the dielectric and piezoelectric properties of the ceramics. So reagent grade metal oxides or carbonate powders: Na_2CO_3 (99.95%, International Laboratory USA), K_2CO_3 (99%, Panreac Quimica SA), Li_2CO_3 (99+%, International Laboratory USA), CeO_2 (99.99%, International Laboratory USA), Bi_2O_3 (99.9%, Acros Organics USA), TiO_2 (99.9%, Alrich USA), and $CaCO_3$ (99%, International Laboratory USA) were used as raw materials in this project. Before the use, all the powders were heated and kept at 110^oC for 2 h to remove the moisture.

The powders in the stoichiometric ratio of the compositions were first mixed thoroughly in ethanol using zirconia balls for 10 h. The powder was then dried and pressed in disk form and calcined for 2 h at 850 ^{o}C for CBT and at 800 ^{o}C for MBT. For preparing the CBT-Cu-x samples, different amounts of CuO were added and mixed together with the powders before the calcination. The temperature profile for calcining the samples is shown in Figure 2.3. The profile was determined empirically such that the calcination temperature was high enough to carry out and complete the reaction and low enough to avoid volatization loss of Bi_2O_3.

Temperature

Calcintion temperature

2 h

3 °C/min   3 °C/min

25 °C

Time
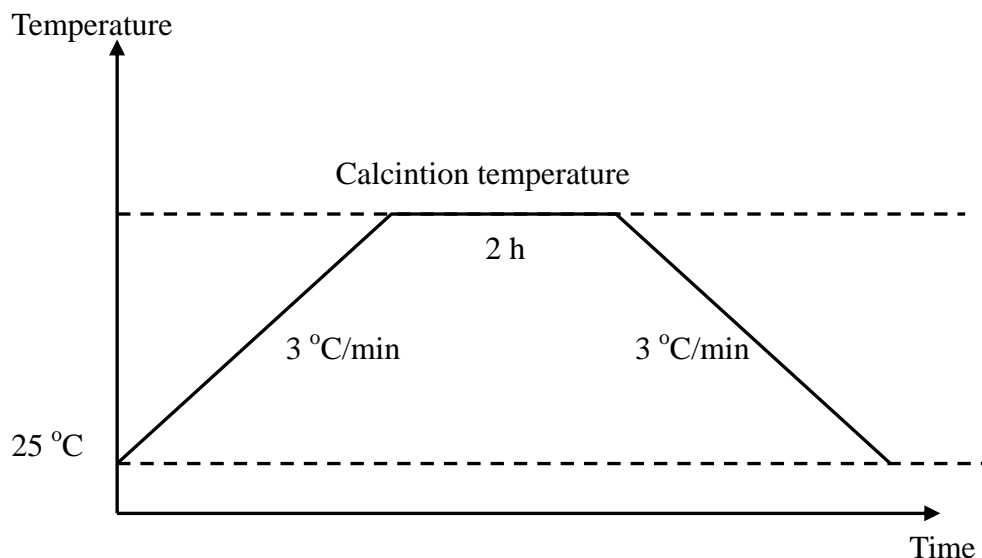
Figure 2.3   Temperature profile for calcining the CBT-based and MBT-based samples.

After the calcination, the samples were grinded and ball milled in ethanol for 16 h. Different amounts of CuO and $BaCO_3$ were also added and ball milled together with the calcinated powders for preparing CBT-Cu/Ba-x and MBT-Cu/Ba-*x* samples.

After the ball-milling, the mixture of the calcined powders and dopants was further mixed thoroughly with a poly(vinylalcohol) (PVA) binder solution using a pair of mortar and pestle. Deionized water was used as a solvent for preparing the solution and the concentration of the solution was about 5 % by weight. The weight ratio of the mixture to the PVA solution is 9:1. The mixed powders were then uniaxially pressed into disk samples with a diameter of 12 mm and a thickness of 0.9 mm. The tool for dry-pressing the (green) disk samples is shown in Figure 2.4.

Before the dry-pressing, a torsion movement was applied to flatten the powder surface. The uniaxial pressure was about 355 MPa. During the dry-pressing, air was driven out and the ceramic powders were well packed and stuck together with PVA. This could improve the sintering reaction by increasing the contact surface area between powders.
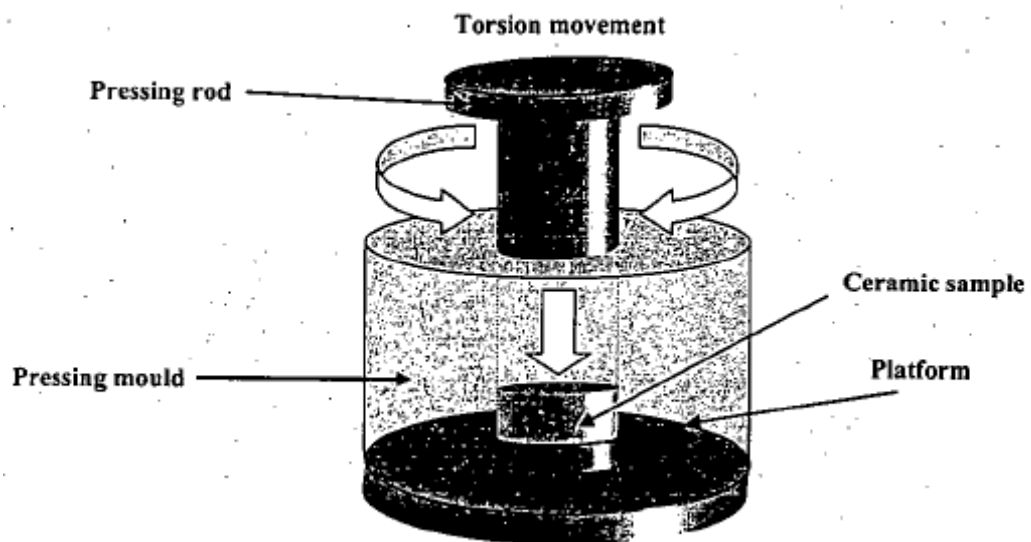
Figure 2.4   Schematic diagram of the tool for dry pressing the disk samples.

Organic binder, such as PVA, should be removed before sintering. To completely burn out the PVA binder and prevent from forming cracks, the samples were heated at $650^{o}C$ for 4 h at a slow heating rate of $1.5\ ^{o}C/min$. The temperature profile for binder removal is shown in Figure 2.5.

Temperature

650 ^{o}C   ⌐ ⌐ ⌐ ⌐ ⌐ ⌐ ⌐ ⌐ ⌐ Binder removal ⌐ ⌐ ⌐ ⌐ ⌐

4h

1.5 ^{o}C/min   2 ^{o}C/min

25 ^{o}C

Time
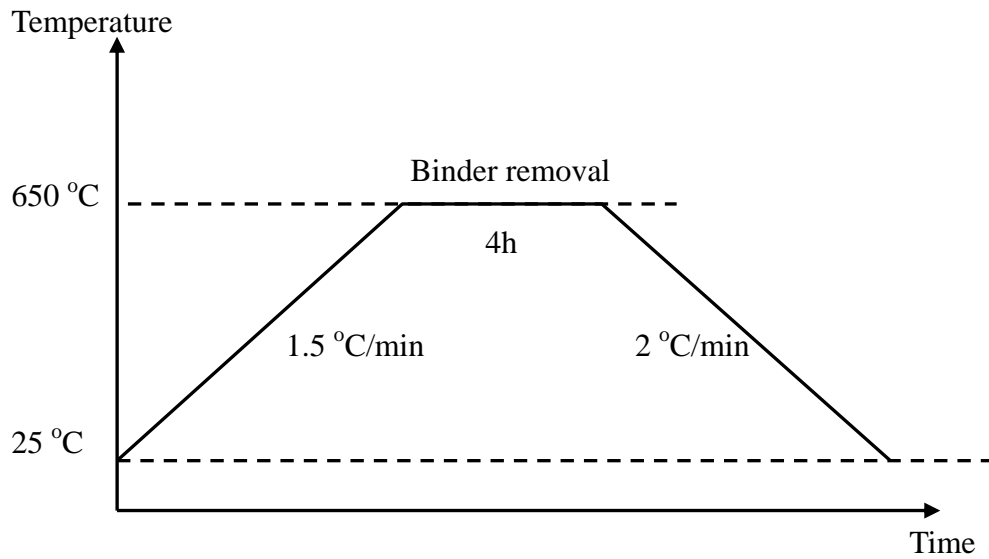
Figure 2.5   Temperature profile for burning out the PVA binder.

After the removal of binder, the samples were sintered in sealed crucible at high temperatures. To reduce volatilization of oxides, the samples were sandwiched between two sintered samples and surrounded by calcined powders as shown in Figure 2.6. The temperature profile for sintering the samples is shown in Figure 2.7. The samples were first heated to 900 ^{o}C with a heating rate of 3°C/min and kept for 1 h, and then further heated to 900 – 1200 ^{o}C with a heating rate of 3 ^{o}C/min. To allow fully grain growth, the samples were kept at the high temperatures for 3-4 h. During sintering, the samples will shrink, porosity will be reduced and mechanical properties can be improved. The mechanism of sintering is schematically illustrated in Figure 2.8. The driving force for sintering is the reduction in the total surface area of particles. Sintering is carried out below melting temperature so that a liquid phase is normally not present. Mass transport necessary to effect the changes shown in Figure 2.8 is accomplished by atomic diffusion from bulk particles to the neck

regions [41].
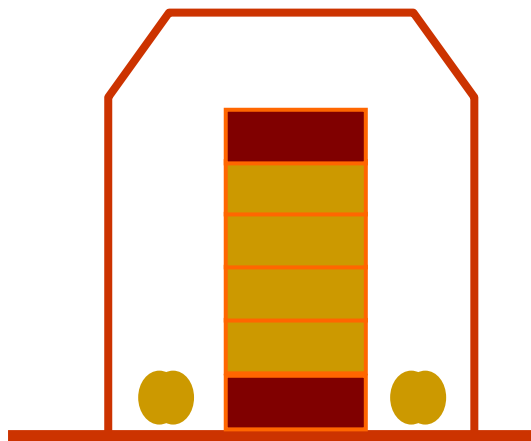
Figure 2.6   Schematic diagram of the setup for sintering the ceramic disks.
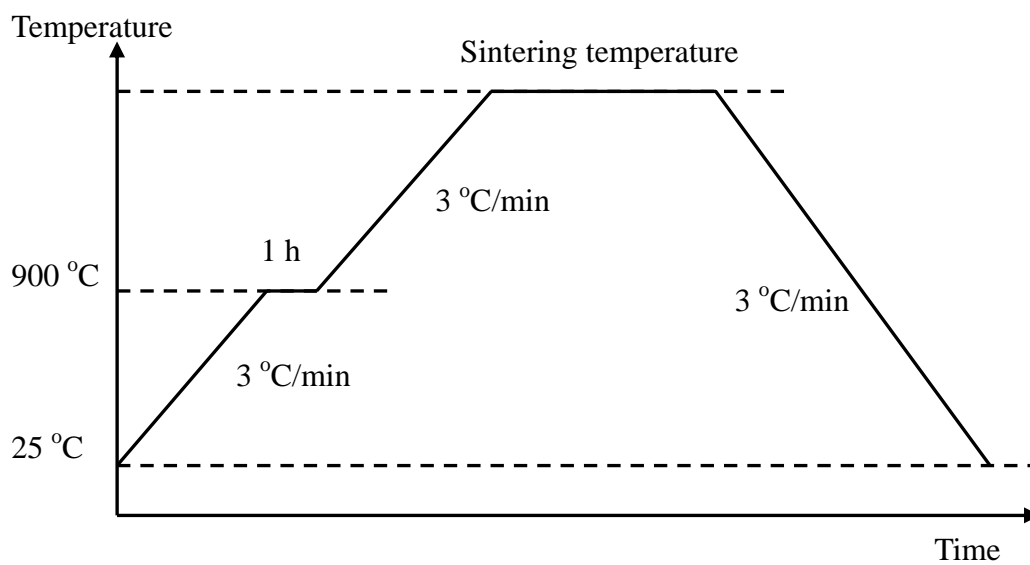
Figure 2.7   Temperature profile for sintering.

(a)

(b)

(c)
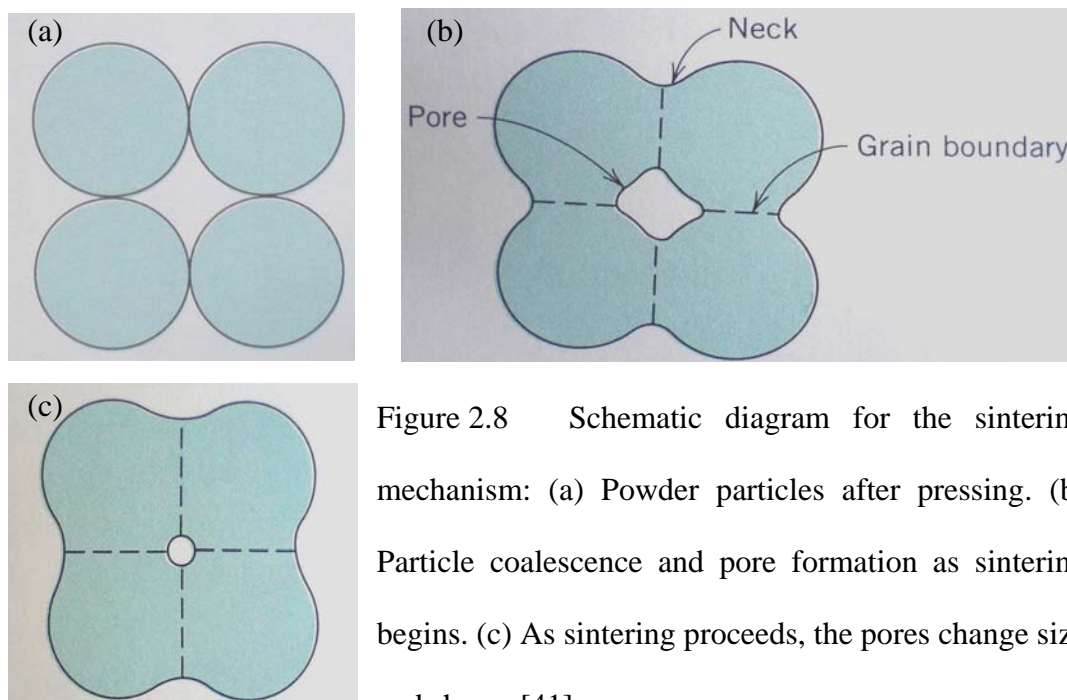
Figure 2.8   Schematic diagram for the sintering mechanism: (a) Powder particles after pressing. (b) Particle coalescence and pore formation as sintering begins. (c) As sintering proceeds, the pores change size and shape. [41]

Because of shrinkage, the thicknesses of the sintered samples may not be uniform. So polishing is required for preparing a ceramic sample with uniform thickness and smooth surface for characterizations. In this work, the sintered samples were polished with wet fine silicon carbide abrasive papers. After that, a thin layer of silver paste was screen printed on the top and bottom surfaces of the samples and fired at 650 $^{\circ}$C for 15 min as electrodes.

2.2.2   Poling

The sintered ceramics do not possess any piezoelectric properties before they are poled under a high electric field. The domains of the as-sintered polycrystalline ceramics are randomly oriented, so the ceramics are isotropic and exhibit no piezoelectric effects. A high dc electric field is required to align the dipoles to

nearly the same direction. After the electric field is removed, a remnant polarization remains, making the ceramics become piezoelectric. The poling field of a material is estimated from its hysteresis loop while the optimum poling temperature and time are determined experimentally. In this work, the CBT-based and MBT-based ceramic samples were poled under a dc field of 12 kV/mm at 220 ^{o}C in a silicone oil bath for 20 min. The poling setup is shown schematically in Figure 2.9. After poling, the ceramic samples were short circuited by wrapping in an aluminum foil at room temperature to remove the charges injected to the sample during the long poling process.
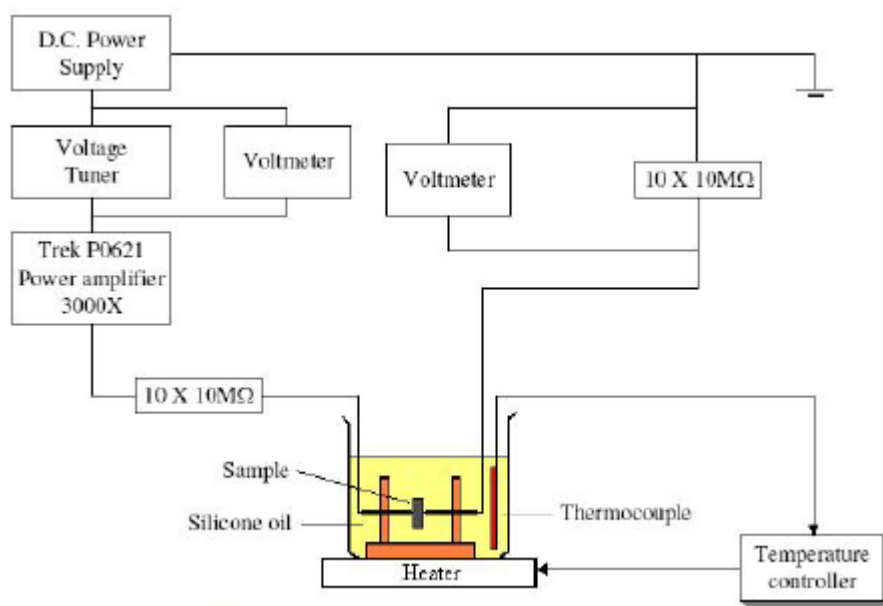
Figure 2.9   Schematic diagram of the poling setup.

2.3 Fabrication of Double-layered Resonators

The schematic diagram of the double-layered resonator is shown in Figure 2.10. As this project aims to develop resonators for high-frequency applications, the thickness of the resonator is designed to be very small, about 0.2 mm. It is expected that the resonance frequency of the resonator is about 20 MHz. In addition, the resonator contains an inner electrode so that it can resonate at the TE2 mode (second harmonic of the thickness extension vibration mode). In view of that, multilayer techniques, including roll-casting, screen-printing, stacking and cofiring, were applied to fabricate the double-layered resonators.
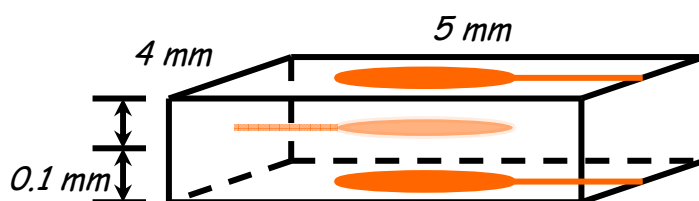
Figure 2.10   The schematic diagram of double-layered resonator

2.3.1   Preparation of Green Thick Sheets by Roll Casting

Similar procedures were applied to prepare calcined powders of the compositions.   After ball milling with suitable amounts of CuO and $BaCO_3$, the mixture was further mixed thoroughly with a PVA binder solution to form a paste. Unlike the one used to prepare ceramic samples, the concentration of the PVA solution was about 22 wt%. In addition, the solution contained 6 wt% of glycerol. The weight ratio of the mixture to the PVA solution is 4:1. Figure 2.11(a) shows the

photograph of the roll cast machine used in this work, while Figure 2.11(b) shows schematically the roll-casting process. The paste was first placed on the rolling cylinders and collected from the bottom as shown in Figure 2.11(b). By repeating the process a number of times with gradually decreasing the cylinder-gap, a green sheet with uniform composition and thickness (~ 0.15 mm) was obtained. To prevent the sheets from drying, they were then stored between a pair of glasses before the next fabrication steps.
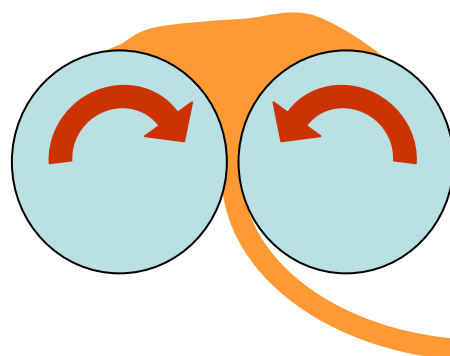
(a)   (b)

Figure 2.11   (a) Photograph of the roll-cast machine. (b) Schematic diagram of the roll casting process

2.3.2   Screen Printing of Inner Electrode and Stacking

The green sheets were cut into small pieces of dimensions 6 mm × 5 mm by a cutting machine.   The photograph of the machine is shown in Figure 2.12. After that, patterned inner electrode (Figure 2.13) was screen printed on the top surface of the samples. As the inner electrode will be co-fired with the green samples at high

temperatures (> 1000°C), the electrode material must have a high melting temperature. In this project, silver/palladium Ag70/Pd30 was used. It is expected that this will help the manufacturers to reduce the cost in mass productions. After the inner electrode was dried, the sample was stacked over by another sample which does not have the inner electrode. The stack was then uniaxially pressed at 150 $^{\circ}$C for 30 min.

Figure 2.12   Photograph of the cutting machine.
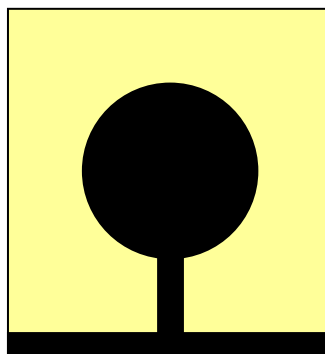
Figure 2.13   The pattern of the inner electrode for the double-layered resonators.

2.3.3   Sintering, Screen Printing of Outer Electrodes and Poling

Similar to the fabrication of ceramic disks, the green samples (the stacks) were sintered in sealed crucible at high temperatures. The samples were sandwiched between two sintered samples and surrounded by some calcined powders as shown in Figure 2.14. As the green samples are very thin (thickness < 0.3 mm), they will bend and twist easily during the high-temperature sintering. Therefore, a dead-weight of 6 g was applied on the top of the samples in order to improve the flatness of the sintered samples. Moreover, in order to prevent solid reaction between the thin green samples, ZrO_2 powders were applied between each green sample.
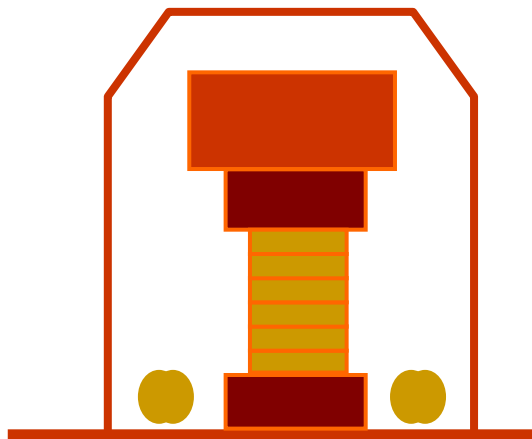
Figure 2.14   Schematic diagram of the setup for sintering of the double-layered resonators.

The same temperature profile shown in Figure 2.7 was used to sinter the

double-layered resonators. After the sintering, patterned electrodes (Figure 2.15) were applied on the top and bottom surfaces of the samples by screen-printing. After firing at 650 ^{o}C for 15 min, the samples were poled in the same manner as the ceramic disks, i.e. connecting the top and bottom electrodes of the sample to the poling setup (Figure 2.9) and applying a dc field of 12 kV/mm for 20 min at 220 ^{o}C.
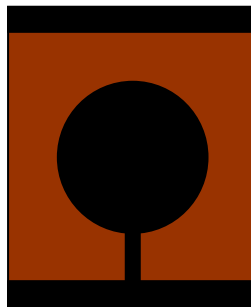
Figure 2.15   The pattern of the outer electrodes for the double-layered resonators.

Chapter Three

Characterizations of the Materials

3.1 Introduction

Before the fabrication of double-layered resonators, the sintering conditions as well as the compositions should be optimized, based on the properties of the samples. In this chapter, characterizations of the ceramic disk samples of different compositions are presented; these include the density measurement, X-ray diffraction (XRD) analysis, scanning electron microscope (SEM), and electrical measurements. The electrical characterizations include ferroelectric hysteresis and piezoelectric measurements.

3.2 Density Measurement

Density measurement is indispensable for evaluating the quality of ceramics. For the density of crystal, the density is as high as the theoretical value. For ceramic, as it is polycrystalline, the density will be lower than the theoretical value and that of crystal. Both the defects such as pore and impurities and improper fabrication conditions such as low sintering temperatures have adverse effects on the ceramic density.

In this project, the density measurement was based on the Archimedes' principle. According to the principle, the mass of the sample in air m_{dry} and the

mass of the sample suspended in water m_{water} were measured using an electronic balance. The density of the sample was calculated by :

$$\rho = \frac{m_{dry}}{m_{dry} - m_{water}} \times \rho_{water}$$

(3.1)

where ρ_{water} is the density of water which is assumed to be 1000 kg/m^3.

3.3 Polarization Hysteresis Measurement

Polarizatoin hysteresis (P-E) loop is one of the most important characteristics of ferroelectric materials. An introduction of the P-E loop has been given in Section 1.2.2 (Figure 1.9). From the P-E loop, the coercive field E_c and remanent polarization P_r of the sample can be obtained.

In this project, the P-E loop was measured using a modified Sawyer Tower circuit [42]. The experimental setup is shown schematically in Figure 3.1. In the measurement, the sample was placed in a silicone oil bath. An ac signal with certain voltage was generated by a function generator (HP 8116A). The signal was amplified by a voltage amplifier (Trek 609D-6) before applying to the sample. The polarization charges generated on the sample was collected by a reference capacitor which was connected in series with the sample and stored in the Sawyer-Tower Circuit Box. In order to minimize the effect on the polarization current, the capacitance of the reference capacitor was chosen to be at least 1000

times larger than that of the sample. The ac input voltage and the voltage across the reference capacitor were measured using a digital oscilloscope (HP 5465A), which was interfaced with a computer for data analysis.
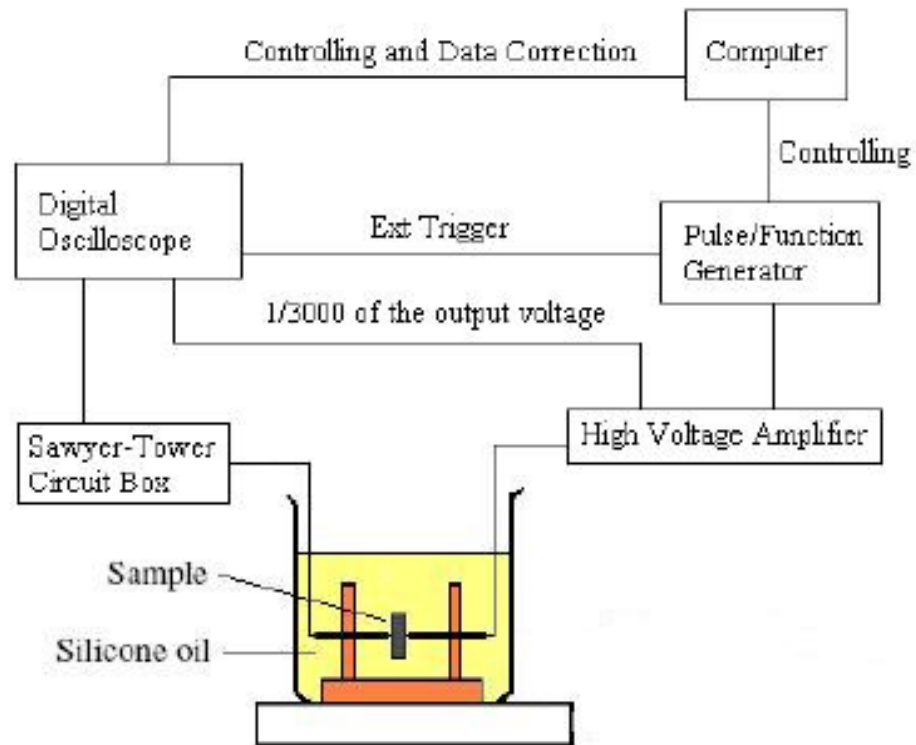
Figure 3.1   Experimental setup for the polarization hysteresis loop measurement.

3.4 Dielectric Properties Measurement

The capacitance C and dielectric loss *tan* δ of the samples were measured at 1 kHz using an impedance analyzer (HP 4294). The relative permittivity ε_r of the samples was then calculated using the following equation:

$$\varepsilon_r = \frac{Ct}{\varepsilon_0 A} \qquad (3.2)$$

where ε_o is permittivity of the free space ($= 8.854 \times 10^{-12}$ F/m), A is the area of the electrode of the sample and t is the thickness of the sample.

Dielectric materials absorb electrical energy under an alternating electric field and thus have dielectric loss. The relative permittivity can be expressed in a complex form:

$$\varepsilon_r = \varepsilon_r' - i\varepsilon_r'' \qquad (3.3)$$

where ε_r' is the real part of the relative permittivity and ε_r'' is the imaginary part. The dielectric loss is given by:

$$\tan\delta = \frac{\varepsilon_r''}{\varepsilon_r'} \qquad (3.4)$$

3.5 Piezoelectric Properties Measurement

In the direct piezoelectric effect, the induced charge is proportional to the force. The effect is characterized by a piezoelectric coefficient d_{ip}^E which is defined (in engineering notation) as

$$d_{ip}^E = \left.\frac{\partial D_i}{\partial T_p}\right|_E \qquad (3.5)$$

where D is the dielectric displacement, E is the electric field and T is the elastic stress, i = 1, 2, 3 and p = 1, 2… 6. Similarly, the converse piezoelectric effect, which is manifested by the induction of the strain under the application of an electric field, is quantified with a piezoelectric coefficient d_{pi}^{T} which is defined as

$$d_{pi}^{T} = \frac{\partial S_p}{\partial E_i}\bigg|_{T} \tag{3.6}$$

where S is the strain. It has been shown that the piezoelectric coefficients d_{ip}^{E} and d_{pi}^{T} were thermodynamically identical [43-44], i.e.

$$d_{ip}^{E} = d_{pi}^{T} \tag{3.7}$$

In the project, d_{33} is measured based on the direct piezoelectric effect using a piezo d_{33} meter (ZJ-3B, Institute of Acoustics, Chinese Academy of Sciences, Beijing). According to Eq. 3.5, an external stress X_3 (in engineering notation, or X_{33} in tensor notation) was applied to the sample, and the charges induced along the 3 axis were measured. The 3 axis was chosen as the poling direction of the samples.

3.6 Resistivity Measurement

Electric resistance is a parameter indicating the energy loss due to the flow of

electric current through the sample. For every device, energy loss should be as small as possible. This is because the more the energy loss, the more heat will be generated and it will affect the performance and the stability of the devices. Therefore, resistivity measurement of materials is important for the selection of materials. The schematic diagram of the resistivity measurement is shown in Figure 3.2.
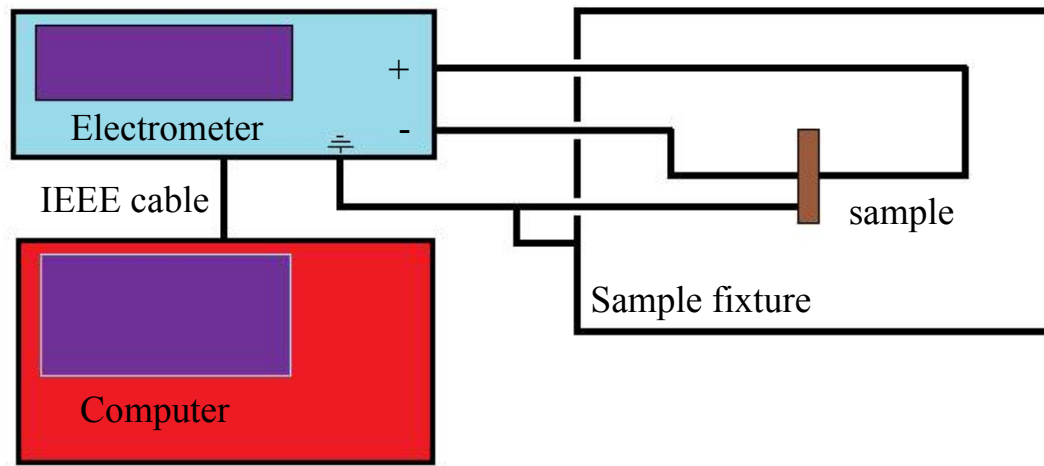
Figure 3.2   Schematic diagram of the resistivity measurement.

Ceramic disk samples with a diameter of 10 mm and a thickness of 0.5 mm were used for the resistivity measurement. In general, due to the high resistivity, the samples have a resistance larger than 200 MΩ. Therefore, guard ring electrode was used to eliminate the current passing through air at the sample edge. The electrode patterns for the resistivity measurement are shown in Figure 3.3. In the measurement, the sample fixture was sealed, and the current was measured by a Keithley 6517A electrometer.
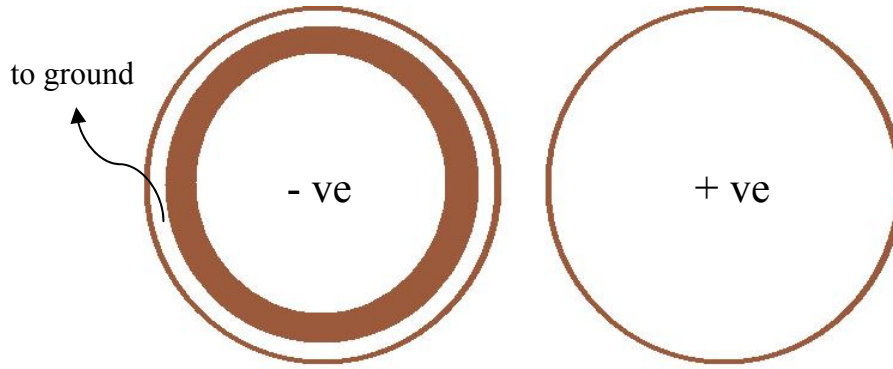
Figure 3.3   The electrode pattern for the resistivity measurement.

3.7 Resonance Characterization

When a poled piezoelectric sample is subjected to an ac signal, various modes of vibration are excited. Because of the changes in dimensions, the corresponding (mechanical) resonance modes can be examined via the measurement of the electrical impedance spectra. In this project, the impedance and phase spectra of the planar mode resonance were measured by an impedance analyzer (Agilent 4294A). The corresponding planar mode electromechanical coupling coefficient k_p was determined following the IEEE standard on Piezoelectricity [7], and the mechanical quality factor Q_m was determined by the equivalent circuit method.

In the measurement, the fundamental parallel resonance frequency f_p, the fundamental and first overtone series resonance frequency (f_s and $f_s^{(2)}$, respectively) were determined from the observed impedance and phase spectra. With the calculated ratio r_s ($= f_s/f_s^{(2)}$), the planar Poisson's ratio σ^P and the parameter η_1 were found from Table 10 of IEEE Std. 176, or equivalently, were calculated using the following binomial equations [45]:

$$\sigma^p = n_0 + n_1 r_s + n_2 r_s^2 + n_3 r_s^3 + n_4 r_s^4 \tag{3.8}$$

$$\eta_1 = m_0 + m_1 r_s + m_2 r_s^2 + m_3 r_s^3 \tag{3.9}$$

where

j	n_j	m_j
0	97.527223	11.2924
1	-126.91730	-7.63859
2	63.400384	2.13559
3	-14.340444	-0.215782
4	1.2312109	-

Then, k_p was calculated as

$$k_p^2 = \frac{\Im(\varphi_1) + \sigma^p - 1}{\Im(\varphi_1) - 2} \tag{3.10}$$

where

$$\varphi_1 = \eta_1 \left(1 + \frac{f_p - f_s}{f_s} \right) \tag{3.11}$$

$\Im$ is the modified quotient of Bessel function defined by

$$\Im(y) = \frac{yJ_0(y)}{J_1(y)} \qquad (3.12)$$

where J_0 and J_1 are the zero and first order Bessel functions of the first kind, respectively, and defined by

$$J_0(y) = \sum_{n=0}^{\infty} \frac{(-1)^n}{n!n!} \left[\frac{y}{2}\right]^{2n} \qquad (3.13)$$

$$J_1(y) = \sum_{n=0}^{\infty} \frac{(-1)^n}{n!(n+1)!} \left[\frac{y}{2}\right]^{2n+1} \qquad (3.14)$$

In calculating the $\Im$ function, it is sufficient to take $n = 10$ in iterating the zero and first order Bessel functions (Eqns. 3.13 and 3.14) for obtaining convergent results. As the ceramic samples have low losses, the series and parallel resonance frequencies are approximately equal to the frequencies of minimum and maximum impedance (f_r and f_a, respectively).

The resonance behavior of the piezoelectric materials can be represented by a lumped-parameter equivalent circuit. Figure 3.4 shows the simplest form of the equivalent circuit where C_o is the free electrical capacitance (at 1 kHz). C_1, L_1 and R_1 are the electrical capacitance, inductance and resistance, respectively, which

represent the converted compliance, effective mass and mechanical loss.
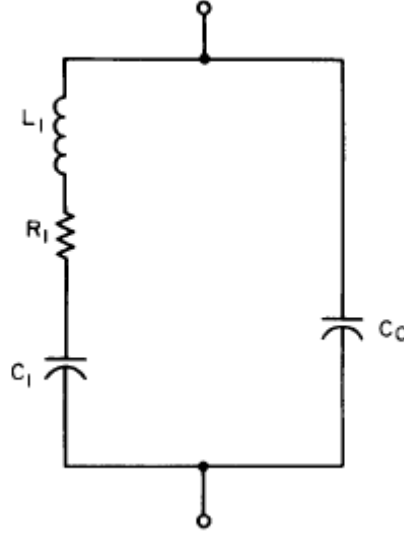
Figure 3.4   Equivalent circuit of a piezoelectric vibrator.

The above equivalent circuit is widely used in the industry to determine the

mechanical quality factor Q_m of the piezoelectric materials, which is defined as the

ratio of the reactance to the resistance in the series equivalent circuit.

In this work, the equivalent circuit parameters C_o, C_1, L_1 and R_1 corresponding

to the radial and thickness mode resonances were determined by the equivalent

circuit analysis function built-in to the Agilent 4294A impedance analyzer, and the

mechanical quality factor Q_m was calculated by:

$$Q_m = \frac{1}{2\pi f_r C_1 R_1} \tag{3.15}$$

3.8 Results and discussions

3.8.1 CBT + *x* wt% CuO Ceramics

The variations of the (optimum) sintering temperature and density ρ with x for the CBT-Cu-x ceramics are shown in Figure 3.5. The optimum sintering temperature was determined as the sintering temperature by which the ceramic had the optimum density and dielectric loss. It can be seen that after the doping of CuO, the observed ρ increases and the sintering temperature decreases slightly. For the CBT-Cu-0.06 ceramic, ρ has a relatively large value of 6942 kg/m^3 and the sintering temperature is decreased, by about 15°C, to 1185°C. Figures 3.6 and 3.7 show, as examples, the SEM micrographs of the CBT-Cu-0 and CBT-Cu-0.06 ceramics. Similar morphologies have been observed for the other ceramics. It can be seen that the ceramics have a dense structure and similar plate-like morphologies. Due to the highly anisotropic layered structure, the grain growth rate along the a(b) axis of CBT are much faster than that along the c-axis. As a result, plate-like grains (with the c-axis oriented normal to the flat surface of the grains) are usually formed in the ceramics. However, as the ceramics are fabricated by pressureless sintering, the orientation of the plate-like grains is random. It is also noted that the grains become smaller after the doping of CuO.
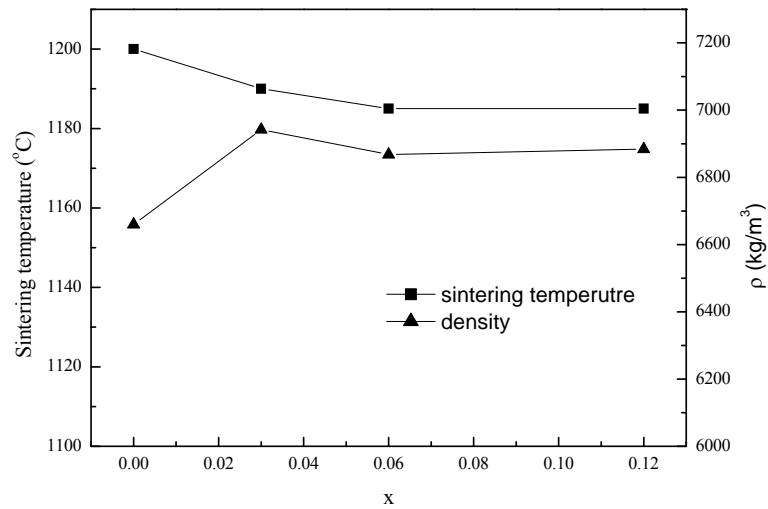
Figure 3.5   Variations of the optimum sintering temperature and density ρ with x

for the CBT-Cu-x ceramics.
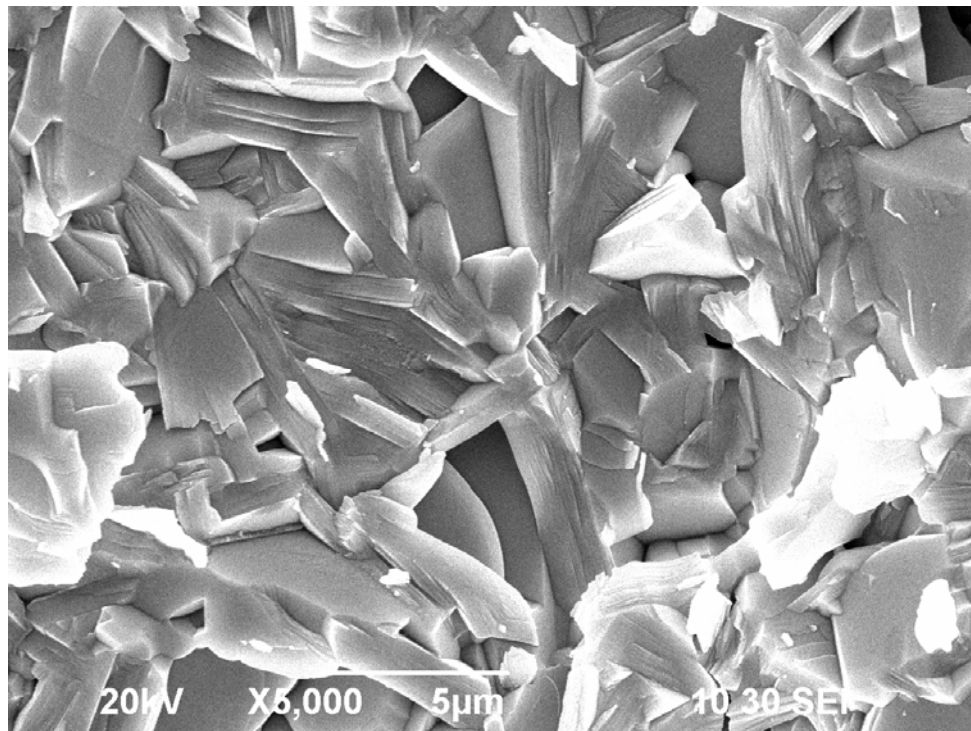
Figure 3.6   SEM micrograph of CBT-Cu-0 ceramic.
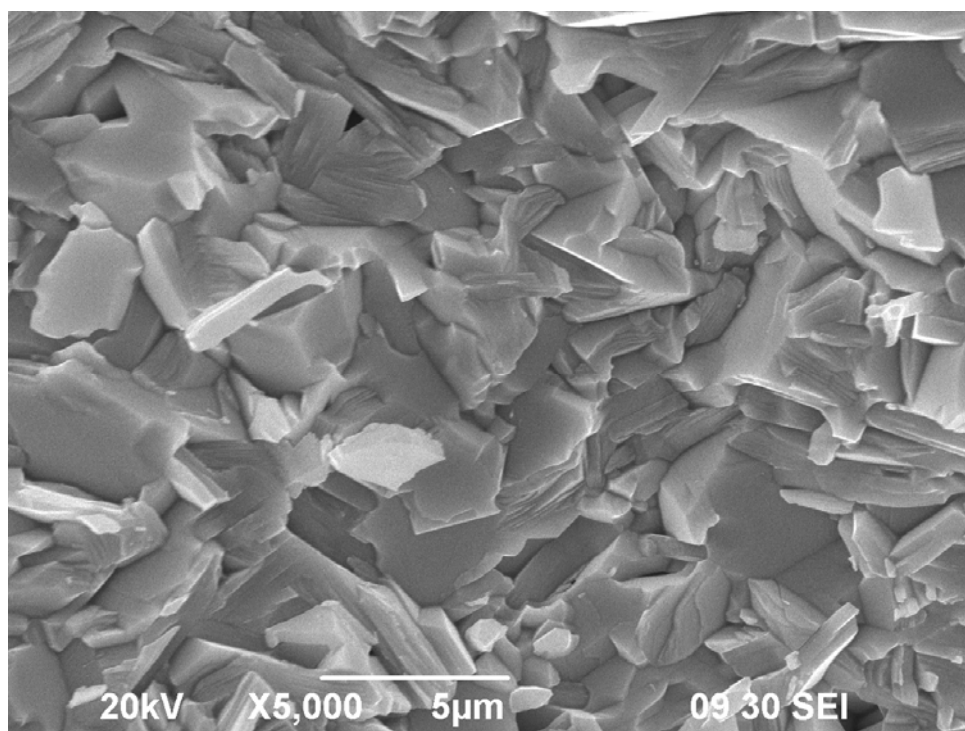
Figure 3.7   SEM micrograph of theCBT-Cu-0.06 ceramic.

The XRD patterns of the CBT-Cu-x ceramics in the range of 2θ from 20° to 60° are shown in Figure 3.8. It can be seen that all the ceramics are of single phase. The peak associated with (1 1 9) plane has the highest intensity, indicating that the ceramics have the bismuth layered structure with m = 4. It has been shown that the most intense diffraction peaks of BLSFs are all of the type of (1 1 2m+1) [35]. Our results (single-phase structure) may suggest that the Cu^{2+} have diffused into the CBT lattices to form a solid solution. The ionic radius of Cu^{2+} is 0.73 Å, which is larger than that of Ti^{4+} (0.68 Å), but smaller than those of Ca^{2+} (1.06 Å) and Bi^{3+} (1.14 Å).   So it may substitute the Ca^{2+} or Bi^{3+}. Indeed, the observation of a single-phase structure may also be due to the small amount of doping (< 0.12 wt%).
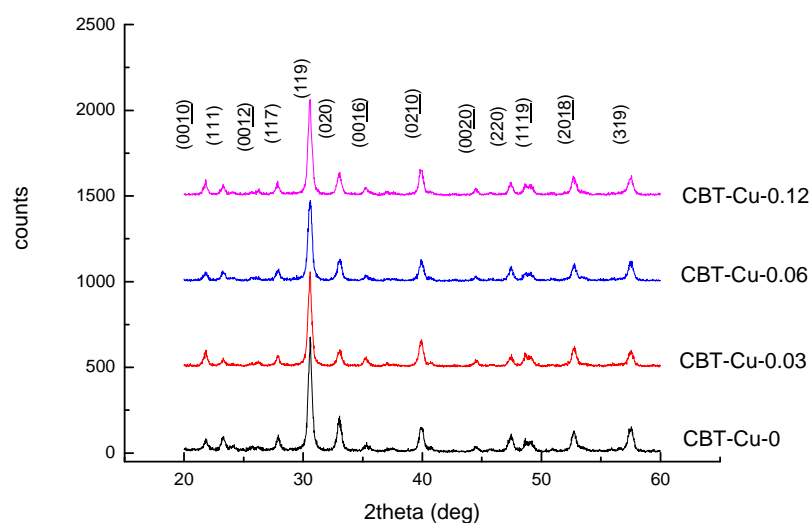
Figure 3.8   XRD patterns of the CBT-Cu-x ceramics in the range of 2θ from 20° to 60°.

The *P-E* loops of the CBT-Cu-x ceramics were measured at room temperature and 220°C, from which the remanent polarization P_r and coercive field E_c were determined. All the ceramics exhibit a typical *P-E* loop at the two testing temperatures. Figure 3.9 shows, as examples, the *P-E* loops of the CBT-Cu-0 and CBT-Cu-0.06 ceramics measured at 220°C. The variations of the observed P_r and E_c with *x* for the ceramics are shown in Figures 3.10 and 3.11, respectively. In general, the observed P_r for each ceramic measured at 220 ^{o}C is larger than that measured at room temperature by about 20 %, while the observed E_c measured at 220 °C is about 40 % smaller than that measured at room temperature. At high temperatures, the dipoles are easier to be switched and alighted along the E-field direction, and hence leading to an increase in P_r and decrease in E_c. On the other hand, at each temperature, P_r decreases with increasing *x*, while E_c remains almost unchanged.

The dc electric field used for poling piezoelectric ceramics is usually chosen as about 2 – 2.5 times of the E_c in order to have a saturated polarization. As shown in Figure 3.13, the E_c for the CBT-Cu-x ceramics is relatively high, about 7 kV/mm even at 220°C. Electrical breakdown occurred easily in the sample at 220°C when the poling field was higher than 13 kV/mm. Therefore, in this project, the CBT-Cu-x ceramics were poled under a relatively low dc electric field of 13 kV/mm ($\sim 2E_c$) at 220 °C for 20 min.
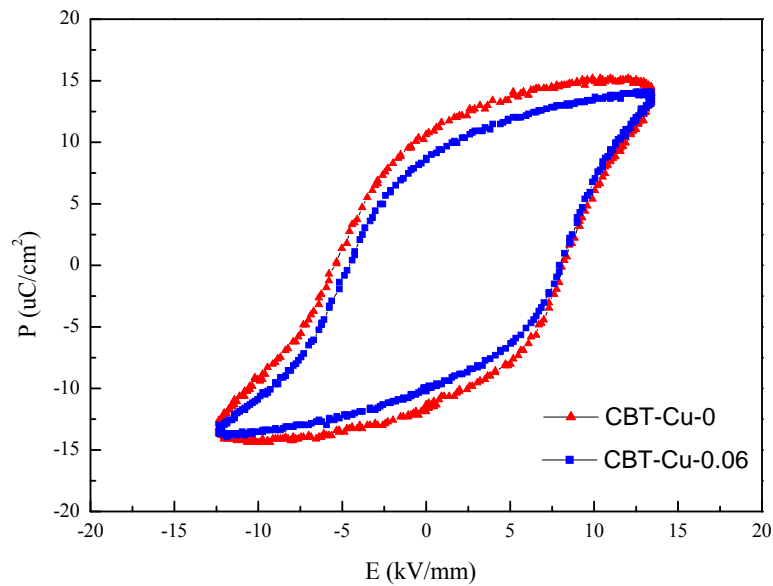
Figure 3.9   *P-E* hysteresis loops of the CBT-Cu-0 and CBT-Cu-0.06 ceramics measured at 220°C.
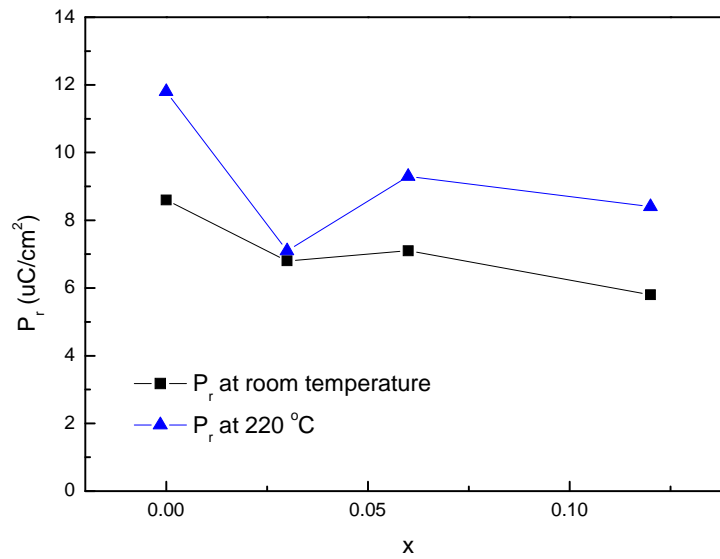
Figure 3.10   Variations of the remanent polarization P_r measured at room

temperature and 220°C with x for the CBT-Cu-*x* ceramics.
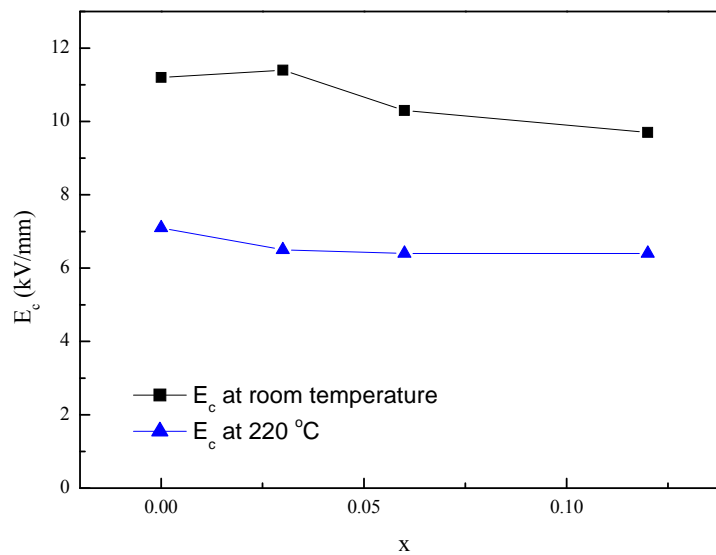
Figure 3.11   Variations of the coercive field E_c measured at room temperature and

220°C with x for the CBT-Cu-*x* ceramics.

The variations of the relative permittivity ε_r and dielectric loss *tanδ* with x for the CBT-Cu-x ceramics are shown in Figure 3.12, while the variation of the resistivity ρ_r is shown in Figure 3.13. After the doping of CuO, the observed ε_r remained almost unchanged at a value around 145. Unlike ε_r, *tanδ* decreases significantly from 0.27 to 0.12% as x increases from 0 to 0.03, and then increases with increasing x. It should be noted that at $x = 0.06$, the observed tanδ is still slightly lower than that at $x = 0$. Consistent with *tanδ*, the resistivity of the ceramics is improved after the doping of CuO. As shown in Figure 3.15, the observed ρ_r increases with increasing x, and then decreases, reaching a maximum value of 3.3×10^{13} Ω·cm at $x = 0.06$.
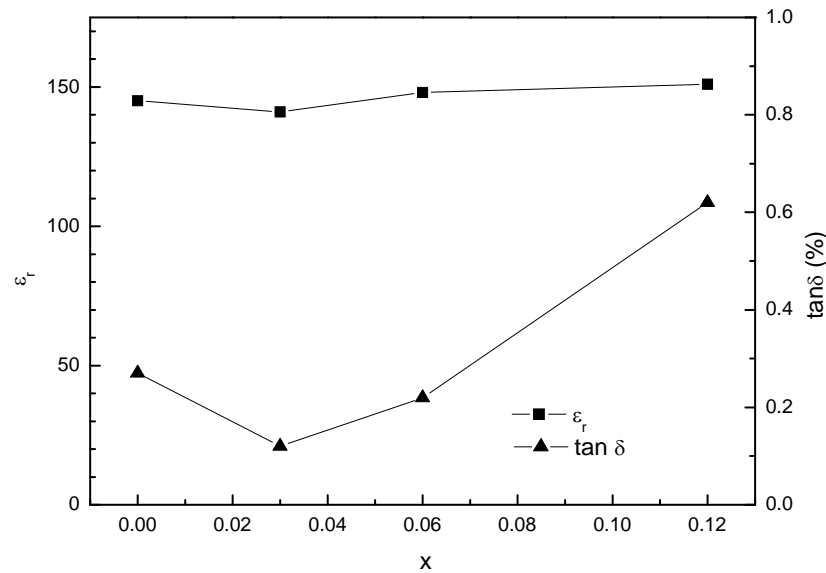
Figure 3.12   Variations of the relatively permittivity εr and dielectric loss tan δ with x for CBT-Cu-x ceramics.
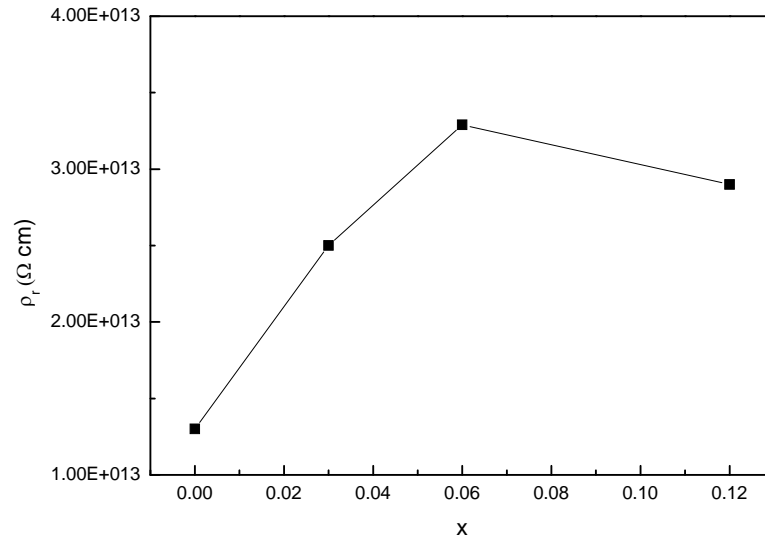
Figure 3.13　　Variation of the resistivity ρ_r with x for the CBT-Cu-*x* ceramics.

The variations of the piezoelectric coefficient d_{33}, planar mode electromechanical coupling coefficient k_p and mechanical quality factor Q_m are shown in Figures 3.14 and 3.15, respectively. As shown in Figure 3.14, the observed d_{33} and k_p increase with increasing *x* and then decrease, giving a optimum value of 12.4 pC/N and 5.1%, respectively, at *x* = 0.03. As compared to a CBT (i.e. CBT-Cu-0) ceramic, these correspond to about 20% and 60% improvement, respectively. Unlike d_{33} and k_p, the observed Q_m decreases slightly with increasing *x* (Figure 3.14). For the CBT-Cu-x-0.03 ceramic, the Q_m is almost unchanged, having a relatively high value of 7400.

On the basis of the above results, it can be seen that the doping of CuO is effective in improving the densification, enhancing the piezoelectric properties and reducing the dielectric losses.
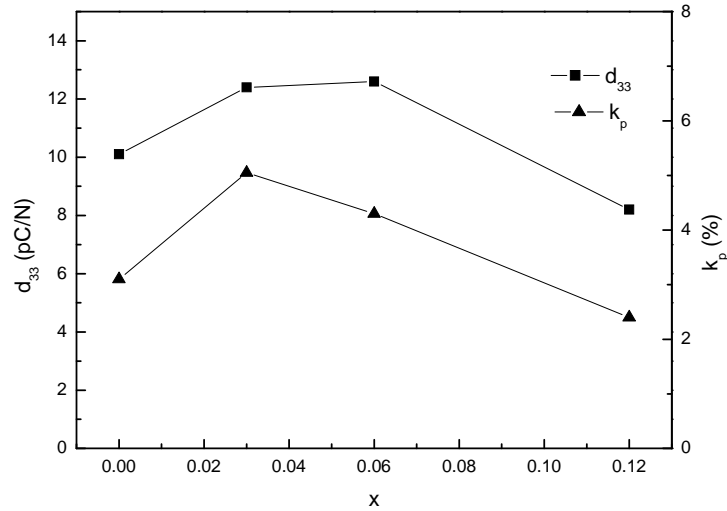
Figure 3.14   Variations of the piezoelectric coefficient d_{33} and planar mode electromechanical coupling coefficient k_p with x for the CBT-Cu-x ceramics.
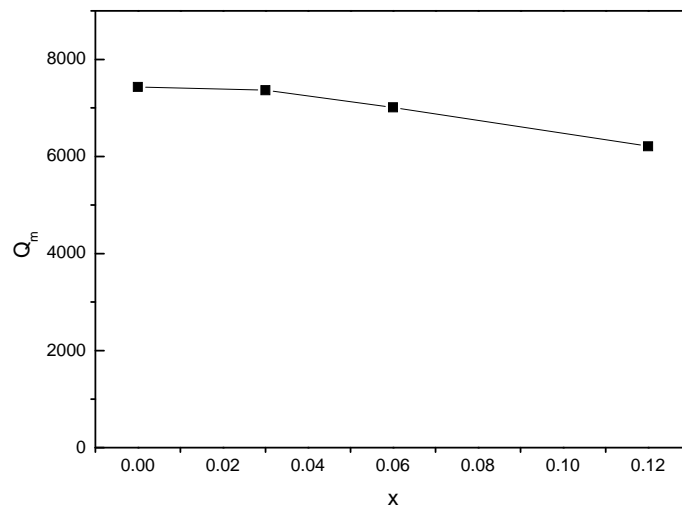
Figure 3.15   Variation of the mechanical quality factor Q_m with x for the CBT-Cu-x ceramics.

3.8.2   CBT + *x* wt% Cu/Ba Ceramics

As mentioned, double-layered resonators with an inner electrode are aimed to be developed. To reduce the production cost, Ag/Pd inner electrode, instead of Pt inner electrode, was used. Therefore, the sintering temperature of the ceramics has to be decreased to around 1000°C. In this project, liquid-phase sintering was applied to lower the sintering temperature of the BLSF ceramics; and the CuO-BaO binary system was selected for this purpose. The phase diagram of the CuO-BaO binary system is shown in Figure 3.16. As shown in Figure 3.16, a eutectic between $BaCuO_2$ and CuO is formed at 890 ^{o}C for the composition comprising 71.5 mol% CuO and 28.5 mol% BaO [26]. Therefore, a complex of Cu and Ba, in the molar ratio of 71.5/28.5, was added to the CBT as well as MBT (discussed in the following section) ceramics in order to decrease their sintering temperatures. As the sintering temperature increases above 890 ^{o}C, a liquid phase will be formed and distributed evenly between the grains of CBT or MBT. This can improve the reaction between the grains and hence densification. As a result, the ceramics can be well-sintered and densified at a lower sintering temperature.
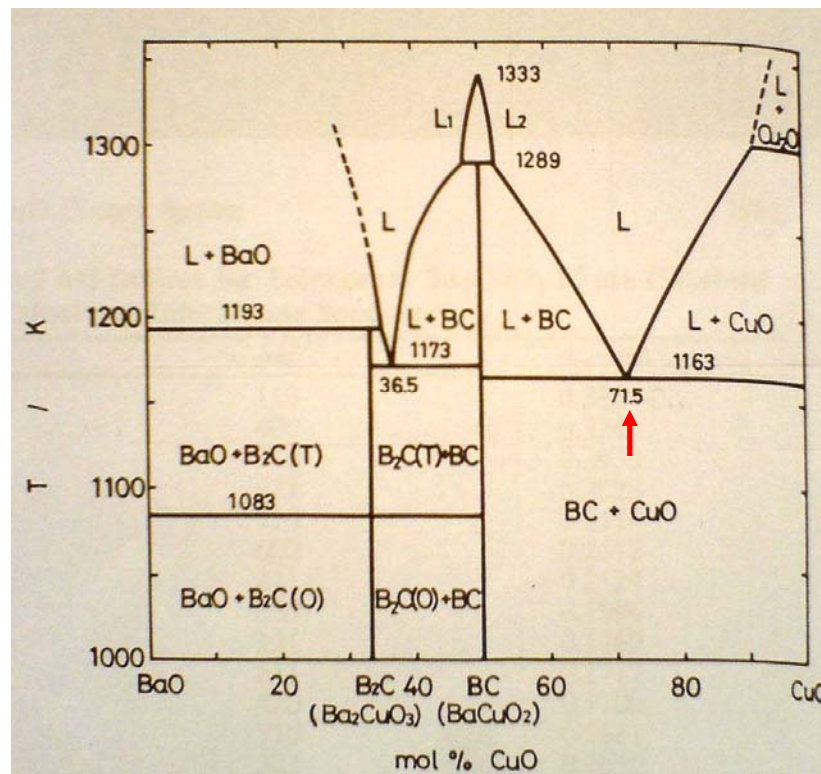
Figure 3.16   Phase diagram of the CuO-BaO binary system. [46]

The variations of the optimum sintering temperature and ρ with x (the wt% of the complex Cu/Ba) for the CBT-Cu/Ba-x ceramics are shown in Figure 3.17. Similar to the CBT-Cu-x ceramics, the optimum sintering temperature was determined as the sintering temperature by which the ceramic had the optimum density and dielectric loss. In general, the sintering temperature decreases almost linearly with increasing x, while the observed ρ increases. It can be seen that at x = 0.30, the sintering temperature is already decreased to below 1000°C. Figure 3.18 shows, as an example, the SEM micrographs of the CBT-Cu/Ba-0.30 ceramic. Similar morphologies have been observed for the ceramics. All the ceramics have a dense structure and similar plate-like morphologies. Probably due to the low sintering temperature ($\sim$1000°C), the grains of the ceramics with $x \neq 0$ become much smaller.

The XRD patterns of the CBT-Cu/Ba-*x* ceramics are shown in Figure 3.19. All the ceramics are of single phase, with the diffraction peaks attributable to a bismuth layered structure with m = 4. Probably due to the small amount of addition (< 0.5 wt%), secondary phases, such as $BaCuO_2$ and CuO, have not been observed.
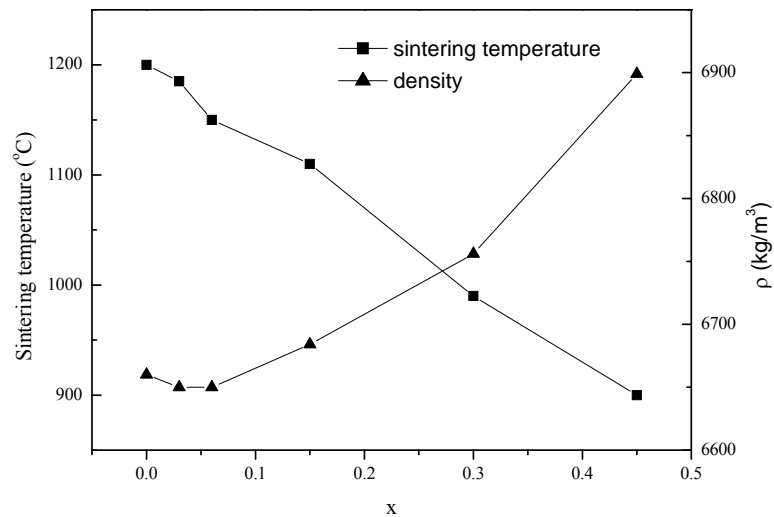
Figure 3.17   Variations of the sintering temperature and density ρ with x for the CBT-Cu/Ba-*x* ceramics.
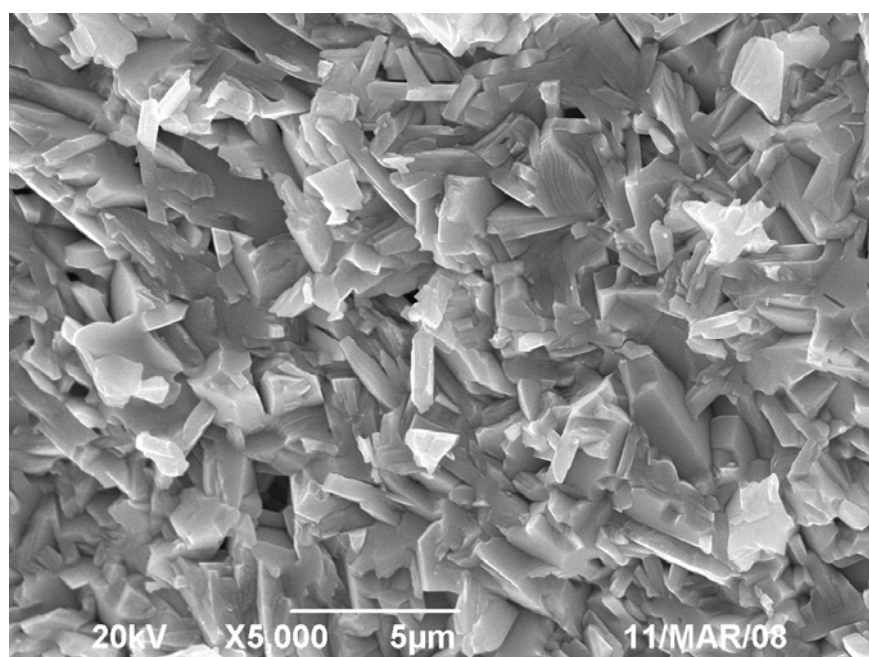
Figure 3.18   SEM micrograph of CBT-Cu/Ba-0.30 ceramic.
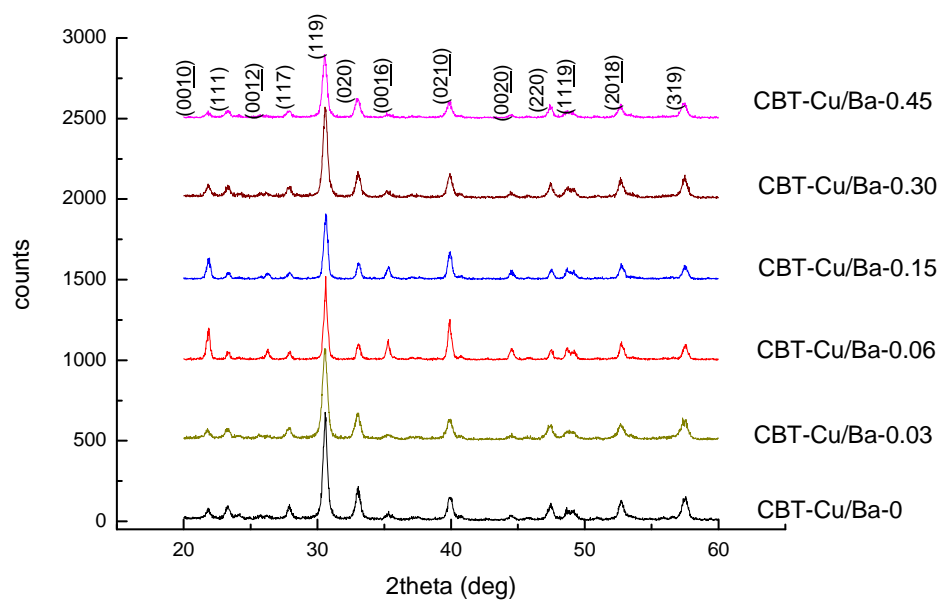
Figure 3.19   XRD patterns of the CBT-Cu/Ba-*x* ceramics in the ranges of 2θ from

20° to 60°.

The P-E loops of the CBT-Cu/Ba-*x* ceramics were measured at 220°C, from which P_r and E_c were determined. All the ceramics exhibit a typical *P-E* loop. Figure 3.20 shows, as examples, the *P-E* loops of the CBT-Cu/Ba-0 and CBT-Cu/Ba-0.30 ceramics. The variations of the observed P_r and E_c with *x* for the ceramics are shown in Figures 3.21 and 3.22, respectively. It can be seen that the observed P_r decreases significantly from 12 to 3.5 $\mu C/cm^2$ as *x* increases from 0 to 0.45, while the observed Ec decreases only slightly from 7 to 5 kV/mm^2. Similar to the CBT-Cu-x ceramics, a relatively low dc electric field of 13 kV/mm (~2E_c) was used to pole the CBT-Cu/Ba-x ceramics at 220 °C for 20 min.
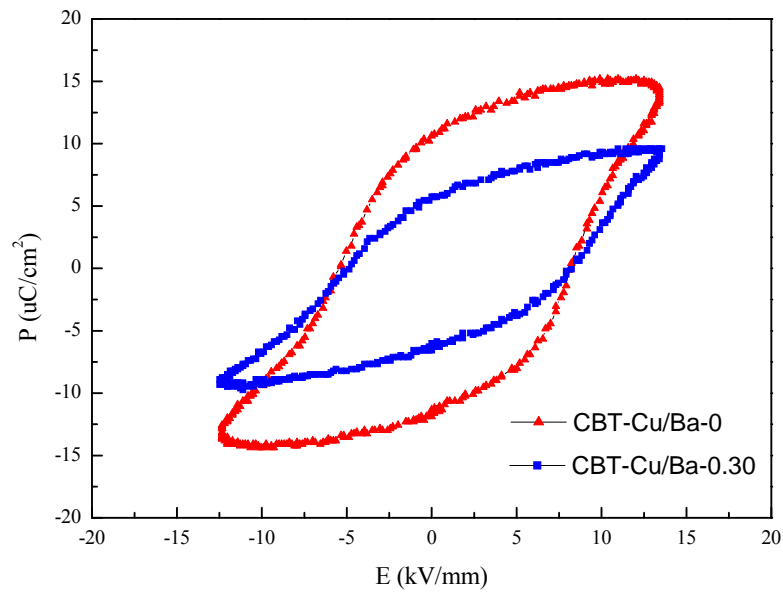
Figure 3.20   *P-E* hysteresis loops of the CBT-Cu/Ba-0 and CBT-Cu/Ba-0.30 ceramics measured at 220 ^{o}C.
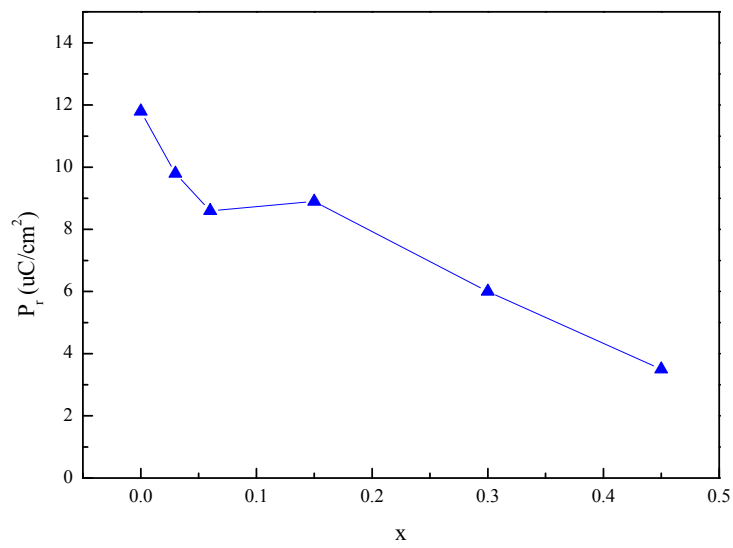
Figure 3.21   Variation of the remanent polarization P_r measured at 220°C with x

for the CBT-Cu/Ba-*x* ceramics.
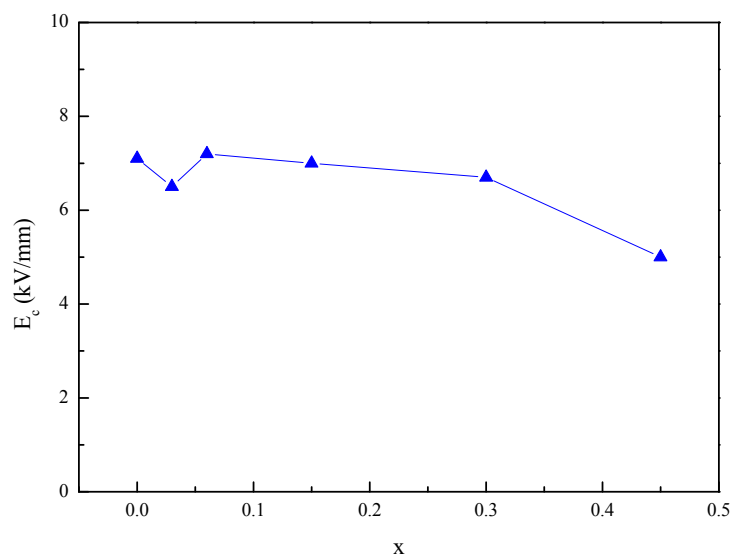
Figure 3.22   Variation of the coercive field E_c measured at 220°C with x for the

CBT-Cu/Ba-*x* ceramics.

The variations of ε_r and *tanδ* with x for the CBT-Cu/Ba-*x* ceramics are shown in Figure 3.23, while the variation of ρ_r is shown in Figure 3.24. As show in Figure 3.23, both the observed ε_r and *tanδ* decrease will increasing x and then increase, giving a minimum value of 132 and 0.12 %, respectively, at $x = 0.06$. Consistent with *tanδ*, the observed ρ_r increases from 1.3×10^{13} to 2.5×10^{13} Ω·cm as x increases from 0 to 0.06 (Figure 3.24). The observed ρ_r remains almost unchanged at larger x. The variations of d_{33} and k_p with x for the CBT-Cu/Ba-*x* ceramics are shown in Figure 3.25, while the variation of Q_m is shown in Figure 3.26. It can be seen that a small amount of the Cu/Ba complex (0.03 wt%) is enough to increase d_{33} significantly from 10 to 15 pC/N and k_p from 3.1 to 4.9%, while Q_m remains unchanged. However, all of them start to decrease at larger x. In general, piezoelectric ceramics prepared by liquid-phase sintering will have degradation in their properties. Therefore, the initial increase in the piezoelectric properties of the CBT-Cu/Ba-*x* ceramics may be arisen from the doping of Cu^{2+} (Figure 3.14).

The thermal-depoling behaviour of the CBT-Cu/Ba-*x* ceramics is shown in Figure 3.27. The poled sample was annealed at elevated temperatures for 1 h, and then its d_{33} value was reevaluated. It can be seen that for the ceramics with $x \leq 0.3$, the observed d_{33} remains almost unchanged at temperatures below 750 °C, and then decreases rapidly to zero at ~900 °C. The decrease in d_{33} is obviously due to the ferroelectric − paraelectric phase transition. Based on our results, the Curie transition temperature T_c for the CBT-Cu/Ba-0 (i.e. CBT) ceramic should be around 800 °C, which is similar to the T_c value determined based on the dielectric-temperature measurement [34]. Accordingly, our results show that the

transition temperature of the CBT-Cu/Ba-x ceramics remains almost unchanged at x ≤ 0.3. T_c is important as it determines the service temperature of the piezoelectric devices, and affects their thermal stability of the performance.

On the basis of the above results, it can be seen that the Cu/Ba complex is effective in decreasing the sintering temperature of the CBT ceramics. Although there is degradation in the piezoelectric and dielectric properties at high addition levels of Cu/Ba, the CBT-Cu/Ba-0.3 ceramic is superior to the CBT ceramic (i.e. CBT-Cu/Ba-0). It should be noted that the CBT-Cu/Ba-0.3 can be well-sintered at a temperature below 1000°C. Therefore, it was selected for the fabrication of the double-layered resonators (Chapter 4).
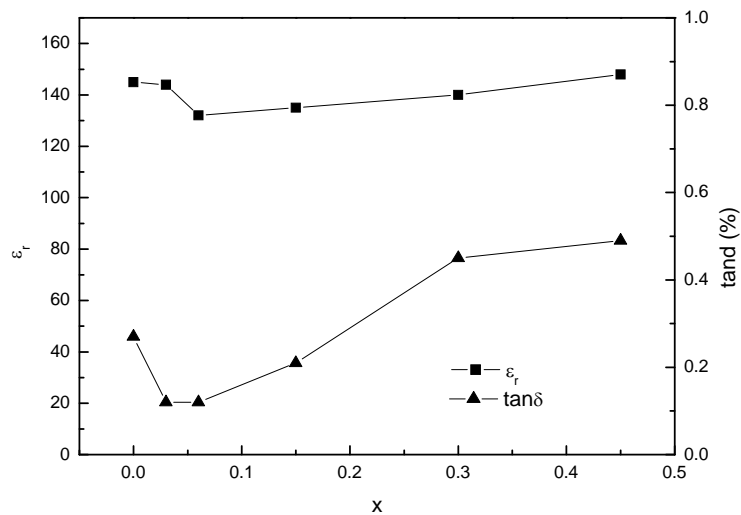
Figure 3.23   Variations of the relative permittivity εr and dielectric loss tanδ for the CBT-Cu/Ba-*x* ceramics.
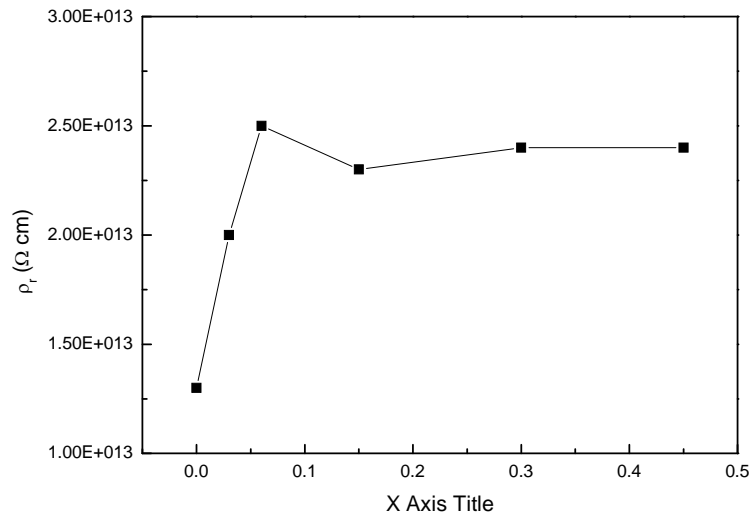
Figure 3.24　　Variation of the resistivity ρ_r with x for the CBT-Cu/Ba-*x* ceramics.
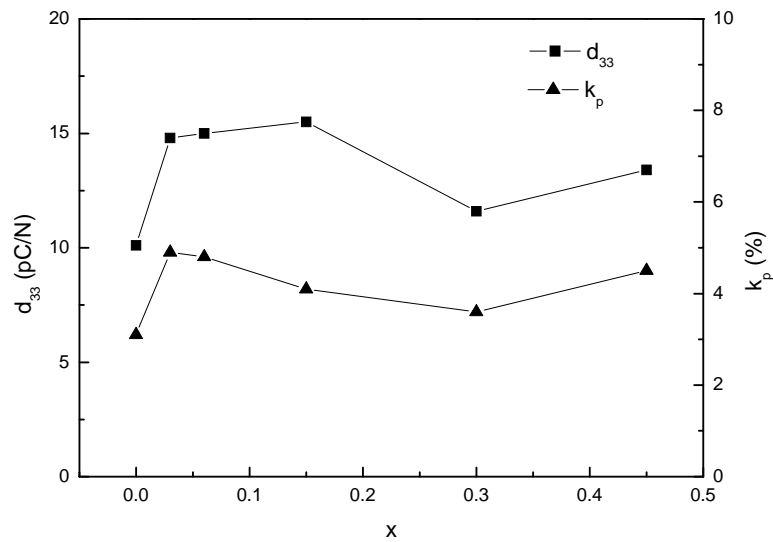
Figure 3.25　　Variations of the piezoelectric coefficient d_{33} and planar mode electromechanical coupling coefficient k_p with x for the CBT-Cu/Ba-*x* ceramics.
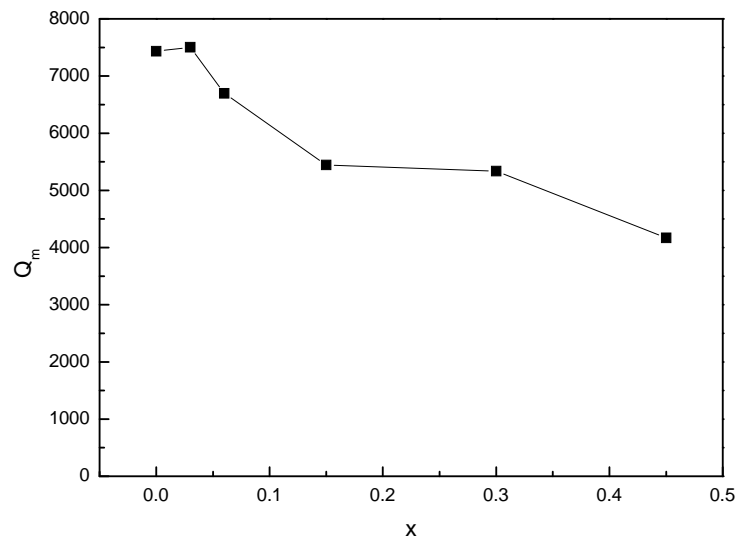
Figure 3.26   Variation of the mechanical quality factor Q_m with the x for the

CBT-Cu/Ba-x ceramics.
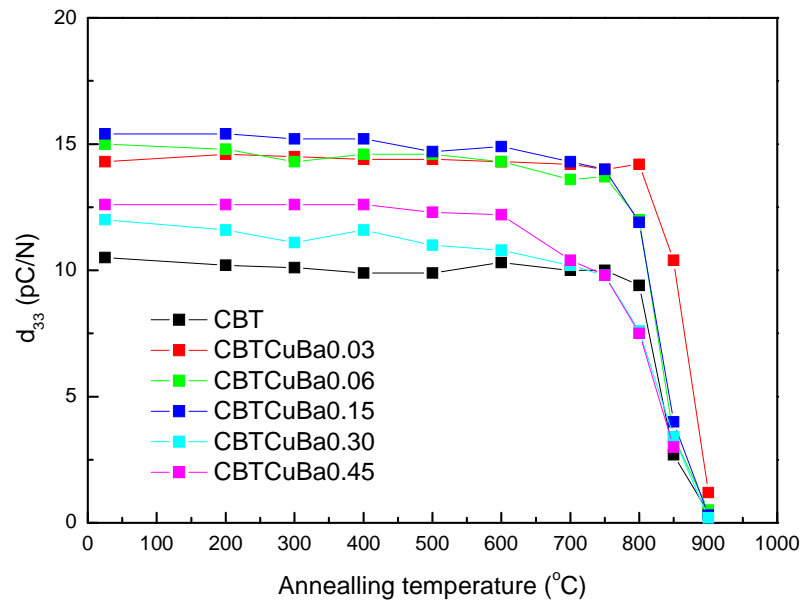
Figure 3.27   Variation of the piezoelectric coefficient d_{33} with the annealing

temperature for the CBT-Cu/Ba-x ceramics.

3.8.3   MBT + *x* wt% Cu/Ba Ceramics

Besides CBT, MBT has also been selected in this project for the fabrication of the double-layered resonators. As compared to CBT, it has a higher piezoelectric coefficient ($d_{33} \sim 28$ pC/N), but a lower T_c. By using MBT, the effect of d_{33} on the performance of a double-layered resonator can be studied. Similar to CBT, the complex Cu/Ba was used to decrease the sintering temperature.

The variations of the optimum sintering temperature and ρ with the *x* for the MBT-Cu/Ba-*x* ceramics are shown in Figure 3.28. Similar to the CBT-based ceramics, the sintering temperature of the MBT ceramics can be decreased by the complex Cu/Ba. As shown in Figure 3.28, the optimum sintering temperature of the MBT-Cu/Ba-*x* decreases with increasing *x*. At *x* = 0.40, the sintering temperature is already decreased to below 1000°C. Probably due to the liquid-phase sintering, the densification of the MBT ceramics is improved after the addition of the Cu/Ba complex. As x increases from 0 to 0.15, the observed ρ increases from 6790 to 7170 kg/m^3. However, at larger *x*, ρ decreases. Figures 3.29 and 3.30 show, as examples, the SEM micrographs of the MBT-Cu/Ba-0 and MBT-Cu/Ba-0.40 ceramics. Similar morphologies have been observed for the ceramics. All the ceramics have a dense structure and similar plate-like morphologies. Probably due to liquid-phase sintering, the grains of the ceramics with $x \neq 0$ become smaller.

The XRD patterns of the MBT-Cu/Ba-*x* ceramics are shown in Figure 3.31. All the ceramics are of single phase, with the diffraction peaks attributable to a bismuth layered structure with m = 4. Similarly, probably due to the small amount

of addition (< 0.50 wt%), secondary phases, such as $BaCuO_2$ and CuO, have not been observed.
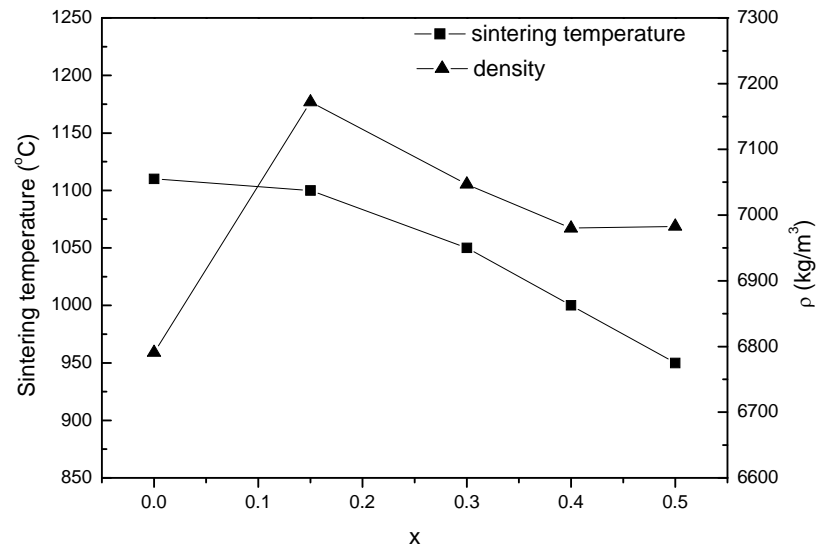
Figure 3.28   Variations of the optimum sintering temperature and density ρ with x

for the MBT-Cu/Ba-*x* ceramics.
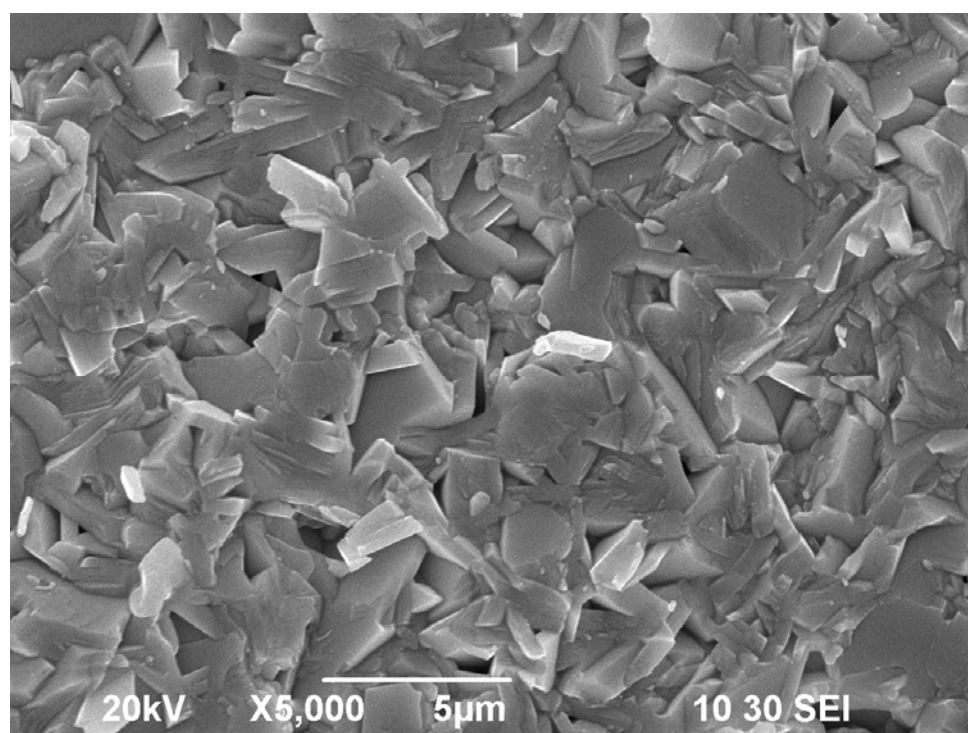
Figure 3.29   SEM micrograph of the MBT-Cu/Ba-0 ceramic.
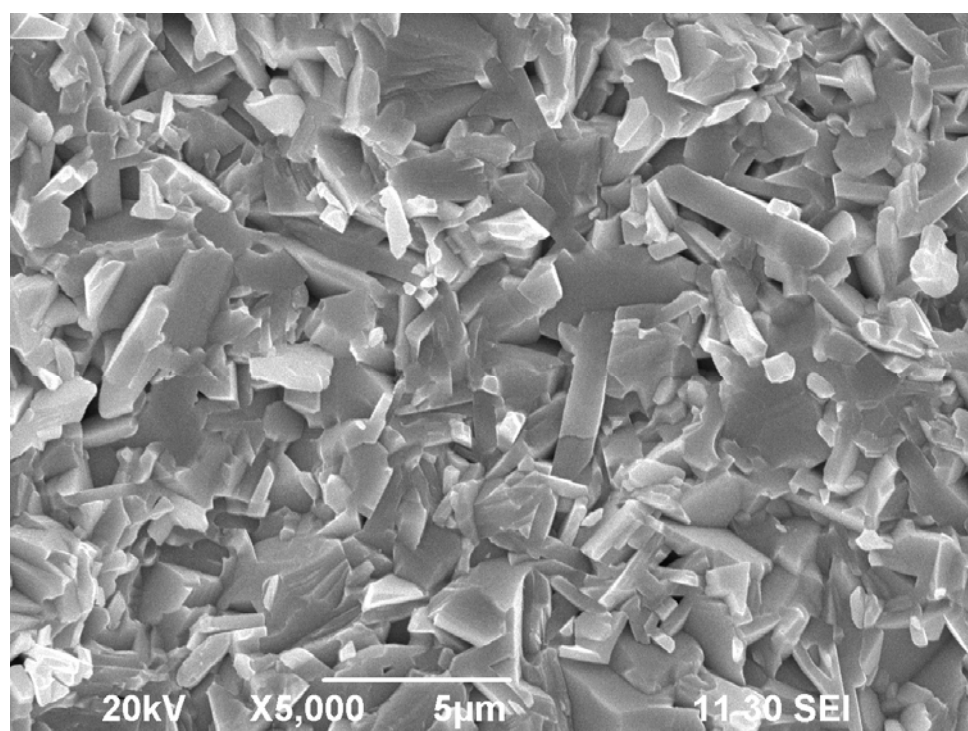
Figure 3.30   SEM micrograph of the MBT-Cu/Ba-0.40 ceramic.
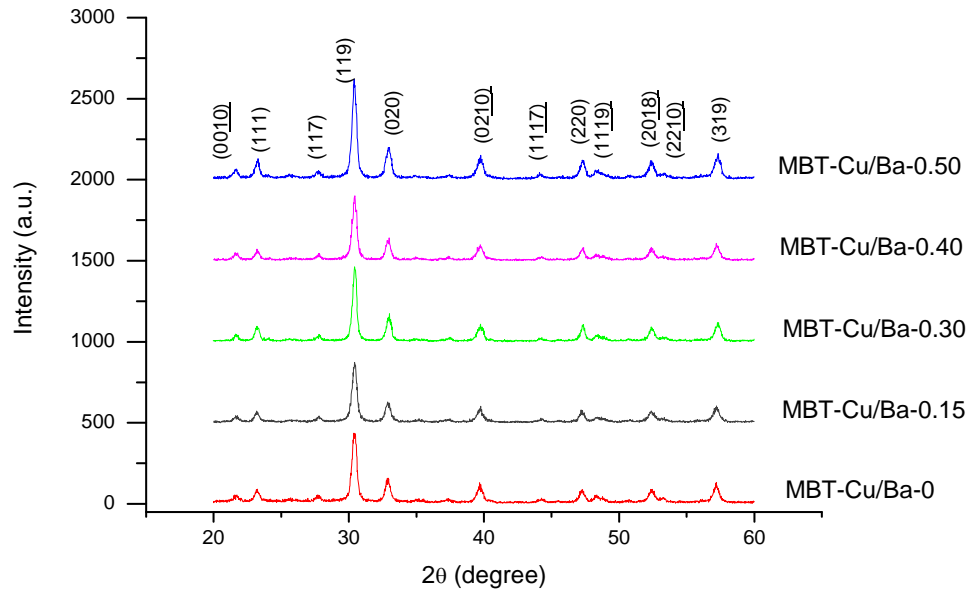
Figure 3.31   XRD patterns of the MBT-Cu/Ba-*x* ceramics in the ranges of 2θ from 20° to 60°.

The *P-E* loops of the MBT-Cu/Ba-*x* ceramics were measured at 220°C, from which P_r and E_c were determined. All the ceramics exhibit a typical *P-E* loop. Figure 3.32 shows, as examples, the *P-E* loops of the MBT-Cu/Ba-0 and MBT-Cu/Ba-0.40 ceramics. The variations of the observed P_r and E_c with *x* for the ceramics are shown in Figures 3.33 and 3.34, respectively. The observed P_r decreases from 5.5 to 4.3 μC/cm^2 as *x* increases from 0 to 0.3, and then increases with increasing *x*. Unlike P_r, E_c remains almost unchanged at a value ~ 5 kV/mm^2. A dc electric field of 13 kV/mm (~2.5E_c) was used to pole the MBT-Cu/Ba-*x* ceramics at 220 °C for 20 min.
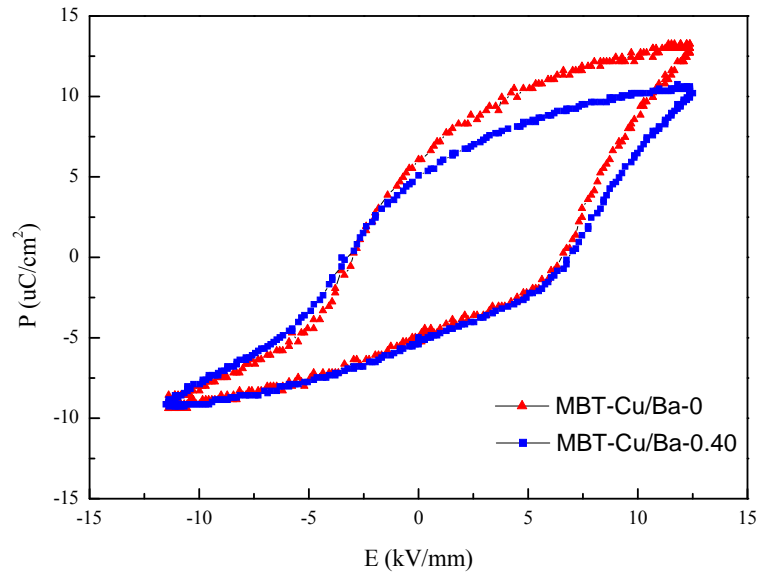
Figure 3.32 *P-E* hysteresis loops of the MBT-Cu/Ba-0 and MBT-Cu/Ba-0.40 ceramics measured at 220 ^{o}C.
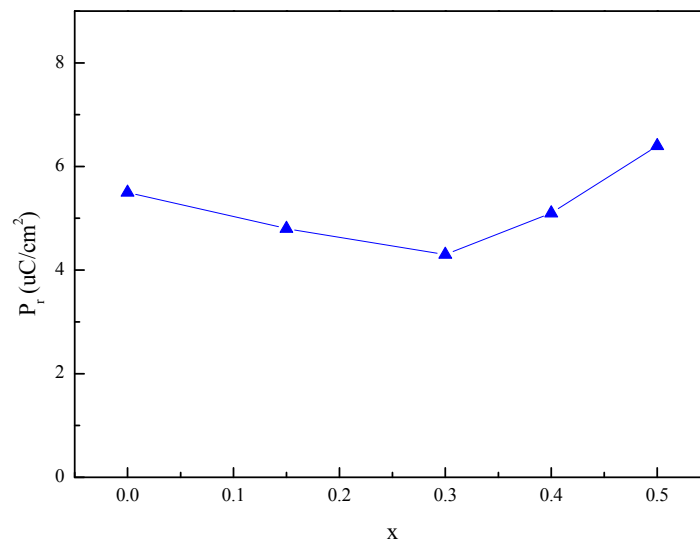
Figure 3.33 Variation of P_r measured at 220 °C with *x* for the MBT-Cu/Ba-*x* ceramics.
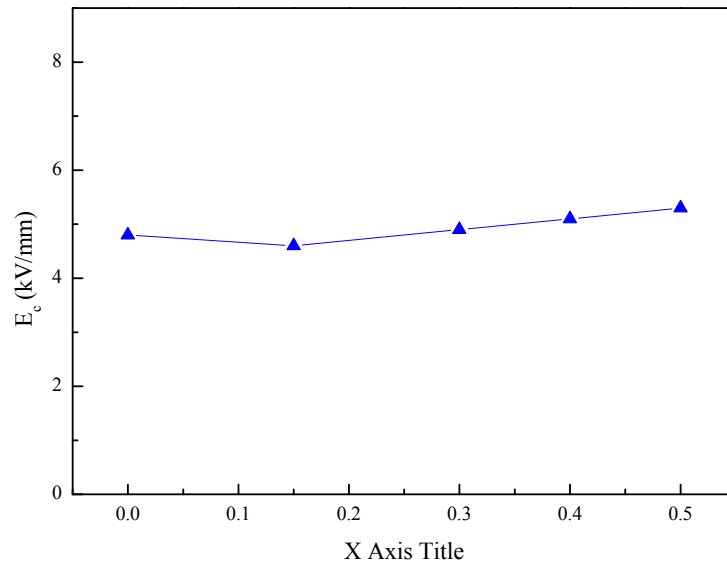
Figure 3.34   Variation of E_c measured at 220 °C with x for the MBT-Cu/Ba-x

ceramics.

The variations of ε_r and $tan\delta$ with x for the MBT-Cu/Ba-x ceramics are shown in Figure 3.35, while the variation of ρ_r is shown in Figure 3.36. As show in Figure 3.35, the observed ε_r remains almost unchanged at ~160 with increasing x, while $tan\delta$ increases almost linearly from 0.16 to 0.45% as x increases from 0 to 0.50. However, the observed ρ_r increases after the addition of the complex Cu/Ba, from 2.2×10^{13} to ~3.0×10^{13} Ω·cm (Figure 3.36). The variations of d_{33} and k_p with x for the MBT-Cu/Ba-x ceramics are shown in Figure 3.37, while the variation of Q_m is shown in Figure 3.38. Unlike CBT-Cu/Ba-x, all d_{33}, k_p and Q_m of the MBT-Cu/Ba-x ceramics decrease generally with increasing x.

The thermal-depoling behaviour of the MBT-Cu/Ba-x ceramics is shown in Figure 3.39. The poled sample was annealed at elevated temperatures for 1 h, and

then its d_{33} value was reevaluated. It can be seen that for the MBT-Cu/Ba-0 ceramic, the observed d_{33} remains almost unchanged at temperatures below 550 °C, and then decreases rapidly to zero at ~750 °C. This indicates that the ferroelectric – paraelectric phase transition of the ceramic is around 600 °C, which is very close to the value determined from dielectric-temperature measurement (620 $^\circ$C) [40]. After the addition of the complex Cu/Ba, there is no significant change in the thermal-depoling behaviour of the ceramics.

On the basis of the above results, it can be seen that the Cu/Ba complex is also effective in decreasing the sintering temperature of the MBT ceramics. Although there is degradation in the piezoelectric and dielectric properties, the MBT-Cu/Ba-0.40 ceramic was selected for the fabrication of the double-layered resonators (Chapter 4). It has a low sintering temperature of 1000°C and a high d_{33} of 24.5 pC/N.
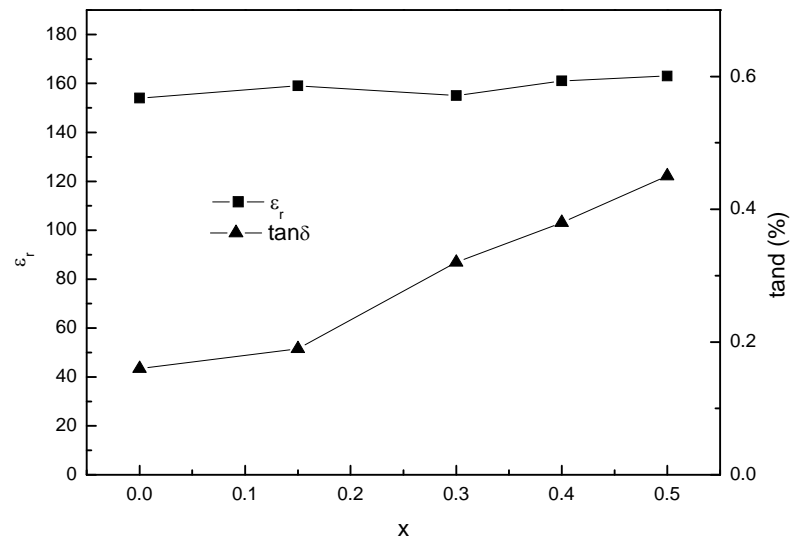
Figure 3.35   Variations of the relative permittivity εr and dielectric loss tanδ with

x for the MBT-Cu/Ba-*x* ceramics.
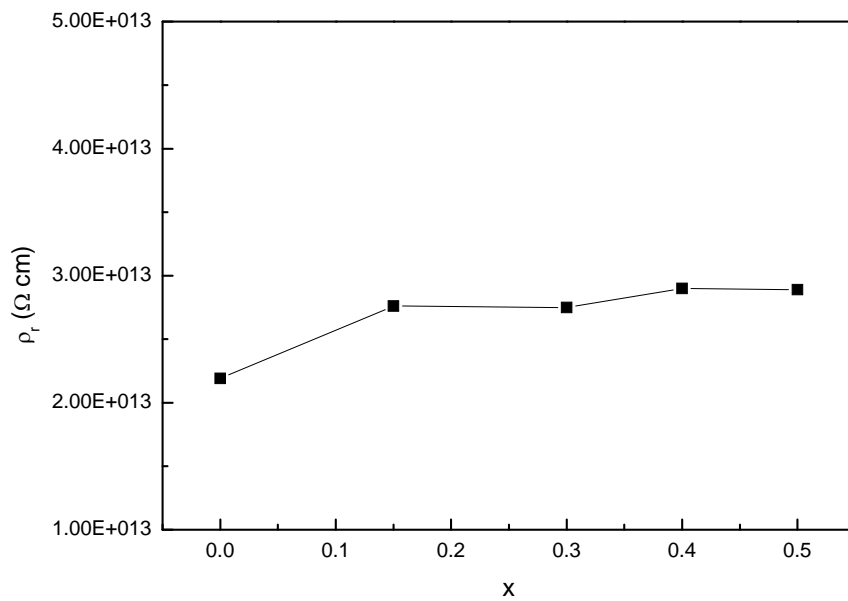
Figure 3.36   Variation of the resistivity ρ_r with x for the MBT-Cu/Ba-*x* ceramics.
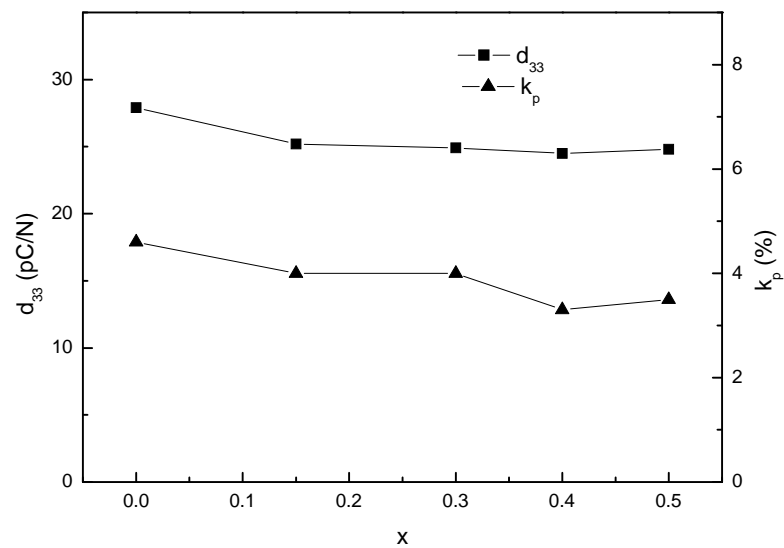
Figure 3.37   Variations of the piezoelectric coefficient d_{33} and planar mode electromechanical coupling coefficient k_p withx for the MBT-Cu/Ba-*x* ceramics.
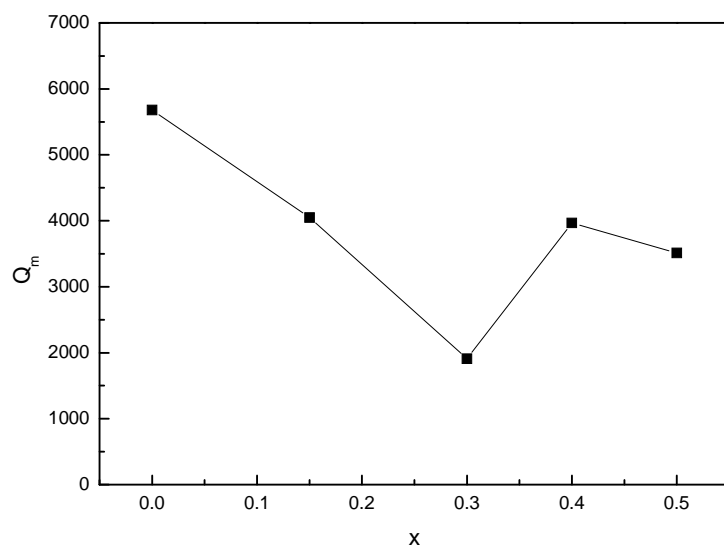
Figure 3.38   Variation of the mechanical quality factor Q_m with x for the MBT-Cu/Ba-*x* ceramics.
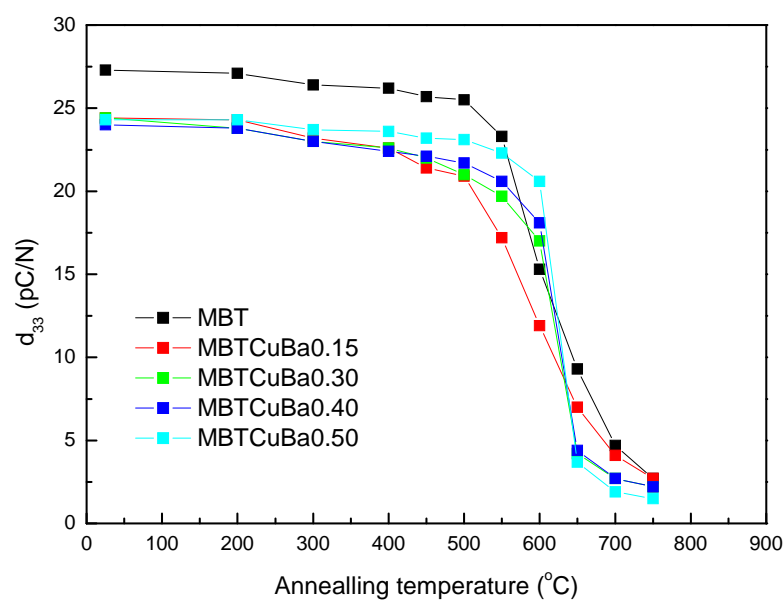
Figure 3.39   Variation of the piezoelectric coefficient d_{33} with the annealing

temperature for the MBT-Cu/Ba-x ceramics.

Chapter Four

Designs and Characterizations of

Double-layered Resonators

4.1 Characterization of Double-layered Resonators

As discussed, double-layered resonators with an Ag70/Pd30 inner electrode are aimed to be developed. Although the Ag/Pd electrode paste can be fired at a temperature up to 1250°C (informed by the manufacturer), our studies have shown that the screen-printed Ag/Pd electrodes should be fired at a temperature below 1000°C; otherwise, the electrodes would shrink, break and hence becomes non-conducting. Therefore, CBT-Cu/Ba-0.30 (i.e. $CaBi_4Ti_4O_{15}$ + 0.30 wt% Cu/Ba) and MBT-Cu/Ba-0.40 (i.e. $[(Na_{0.5}K_{0.5})_{0.94}Li_{0.06}]_{0.5}Bi_{4.5}Ti_4O_{15}$ + 0.5 mol% CeO_2 + 0.40 wt% Cu/Ba) ceramics were selected for the fabrication of the double-layered resonators in this project. Because of the complex Cu/Ba (in the molar ratio of 71.5/28.5), both the ceramics can be well-sintered at a temperature ~1000°C.

Following the procedures described in Chapter 2, double-layered resonators with an inner electrode (Figure 2.13) and outer electrodes (Figure 2.15) using CBT-Cu/Ba-0.30 and MBT-Cu/Ba-0.40 were fabricated. For each composition, resonators with 2-mm and 3-mm electrodes (in diameter) were fabricated. After the fabrication, the resonators were poled (by applying a dc electric field between the top and bottom outer electrodes) using the same conditions for the ceramic disk samples. As the double-layered resonators were prepared from the green sheets

fabricated by the roll-casting method, in which a PVA binder solution with a higher concentration was used, the physical properties of the sintered ceramic sheets may degraded because of the "loose" structure arisen from the "excess" organic chemicals. Therefore, in this project, the piezoelectric and dielectric properties of the "double-layered resonators" (before the connection of the top and bottom electrodes and extension of the inner electrode, discussed below) were evaluated in order to ensure that they have similar properties to those the ceramic disk samples.

To excite the TE2 mode (second harmonic of the thickness extension mode) vibration, the top and bottom electrodes were electrically connected at the edge using quick-dry silver paint as shown in Figure 4.1. The inner electrode was also extended to the other edge for the measurement of the resonance characteristics. To minimize the loading effect on the vibration, the resonator was connected to the equipment through the contacts at the edges (Figure 4.1).
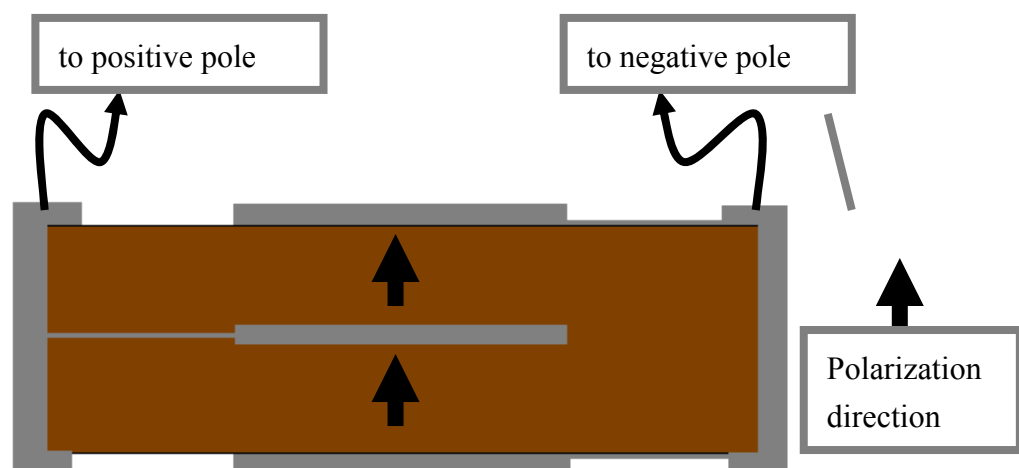
Figure 4.1   Schematically diagram of the double-layered resonators showing the polarization direction and the electrical connections for the characterization.

4.2 Effect of Electrode Size

.   The observed piezoelectric coefficient d_{33} of the CBT-Cu/Ba-0.30 and MBT-Cu/Ba-0.40 "double-layered resonators" (before the connection of the top and bottom electrodes and extension of the inner electrode) are about 11 and 26 pC/N, respectively, while their dielectric loss $tan\delta$ are 0.45 and 0.40% respectively. All these values are similar to those of the ceramic disk samples. Although the double-layered resonators have higher relative permittivity than the ceramic samples (Table 4.1), they should be of good properties for the resonator applications.

Table 4.1   Relative permittivity ε_r of the two compositions in different forms: ceramic disk and double-layered resonators. The relative permittivity is calculated from the observed capacitance, without considering the leakage of electric field at the edges.

	Ceramic disk (full electrode)	Double-layered resonator (3-mm electrode)	Double-layered resonator (2-mm electrode)
CBT-Cu/Ba-0.30	140	152	161
MBT-Cu/Ba-0.40	161	167	173

All d_{33}, ε_r and $tan\delta$ are the intrinsic properties of the materials, so they should be independent of the geometry of the samples. For the d_{33} and $tan\delta$ measurements, the geometrical factors are cancelled so that the observed values can represent the properties of the samples. It seems that the geometrical factors have also been

cancelled in the calculation of ε_r from the observed value of the sample capacitance. However, there are other important effects arisen from the geometry, in particular the area of the electrodes, which have usually been neglected.

In general, ε_r is calculated from the capacitance, electrode area and thickness of the sample using Equation 3.3, in which all the electric field lines are assumed to be confined between the top and bottom electrodes. However, there is leakage of electric field, called stray field lines, at the edge of the electrodes. Figure 4.2 shows schematically the field lines, including the stray field lines, between a pair of electrodes. The observed capacitance of the sample includes the contribution from these stray field lines. If it is neglected in the calculation (e.g. using Equation 3.3), there will be an error in the calculated ε_r. Obviously, the error is strongly dependent on the leakage of the electric field.
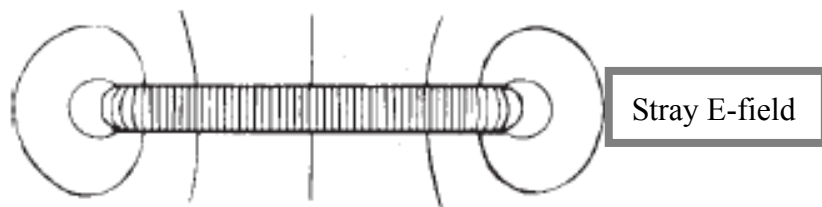
Figure 4.2   Distribution of the electric field lines in a parallel-plate capacitor.

It has been known that the leakage of electric field is controlled by the environment at the electrode edge. Figure 4.3 shows two typical electrode configurations widely used for the ε_r measurement. Figure 4.3(a) is the one for a sample with the top and bottom surfaces fully covered by electrodes, which is also the configuration used in this project for measuring the ε_r of the ceramic disk

samples. For this case, the ratio of the permittivity of the sample to that of air (environment at the electrode edge), i.e. the ε_r of the sample, is one of the major factors controlling the leakage. If ε_r is much larger than 1, most of the electric field lines will be confined within the sample and the leakage becomes negligible. This is true for the lead-based piezoelectric ceramics, e.g. PZT. Otherwise, the electric field will leak significantly to the air. The other configuration is the sample with the top and bottom surfaces covered with partial electrodes (Figure 4.3(b)), which is the configuration used in this project for the double-layered resonators. For this case, the electric field will leak certainly to the environment which is the sample itself, because of the same ε_r. The leakage will then be dependent on the electrode size and sample thickness.

(a)   (b)

Figure 4.3   Two typical electrode configurations for the ε_r measurement: (a) sample with full electrodes; and (b) sample with partial electrodes.

It has been experimentally shown that the ε_r of a sample with either configuration can be correctly calculated by the following equations:

$$\varepsilon_r = \frac{C + C_e}{C_v} \tag{4.1}$$

where C is the observed capacitance of the sample, C_e is the correction for stray

capacitance, and C_v is the direct inter-electrode capacitance in vacuum given by:

$$C_v = \varepsilon_o \frac{A}{t} \tag{4.2}$$

For the sample with full electrode (i.e. Figure 4.3(a)), C_e is given as:

$$C_e = (0.0087 - 0.00252 Int)P \tag{4.3}$$

For the sample with partial electrode, C_e is given as:

$$C_e = (0.0019\kappa_x' - 0.00252 Int + 0.0068)P \tag{4.4}$$

where A is the area of the electrode, t is the thickness of the sample, P is the perimeter of the electrode, κ_x' is the approximate value of the specimen permittivity (estimated from C) [47].

Figures 4.4 shows the % error calculated using Equations 4.1 – 4.4 for electrode configurations used in this project, i.e. ceramic disk sample covered with full electrodes and double-layered resonator covered with partial electrodes (Figure 4.3). The thickness of the sample used for the calculation is 0.6 mm. It can be seen that the % error for the sample with full electrodes becomes almost zero at $\varepsilon_r > 100$. This indicates that the observed ε_r for the CBT-based and MBT-based ceramic disk samples (~140 and ~160, respectively) has good accuracy. On the other hand, the % error for the samples with partial electrodes is large, even at $\varepsilon_r > 100$. It is also

noted that the % error increases as the diameter decreases. Figure 4.5 shows the % error for samples with the same partial electrodes (2 mm in diameter) but different thickness. It can be seen that, for the same partial electrodes, the % error decreases as the thickness decrease at the same ε_r. This suggests that the leakage of electric field should be considered for the samples with partial electrodes, in particular for the sample with small electrode diameter/thickness ratio.
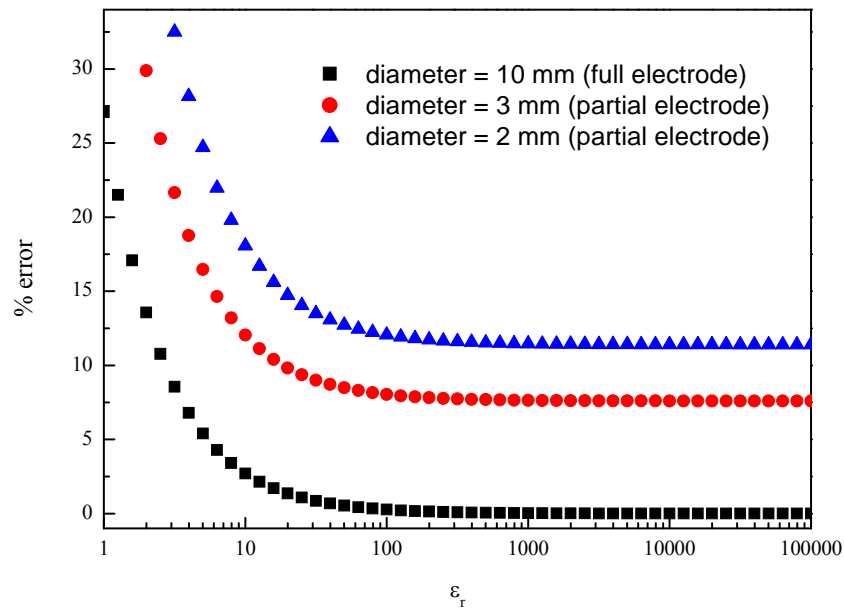
Figure 4.4   Variations of % error with εr for the sample with full electrodes and the samples with partial electrodes. The thickness of the sample used for the calculation is 0.6 mm.
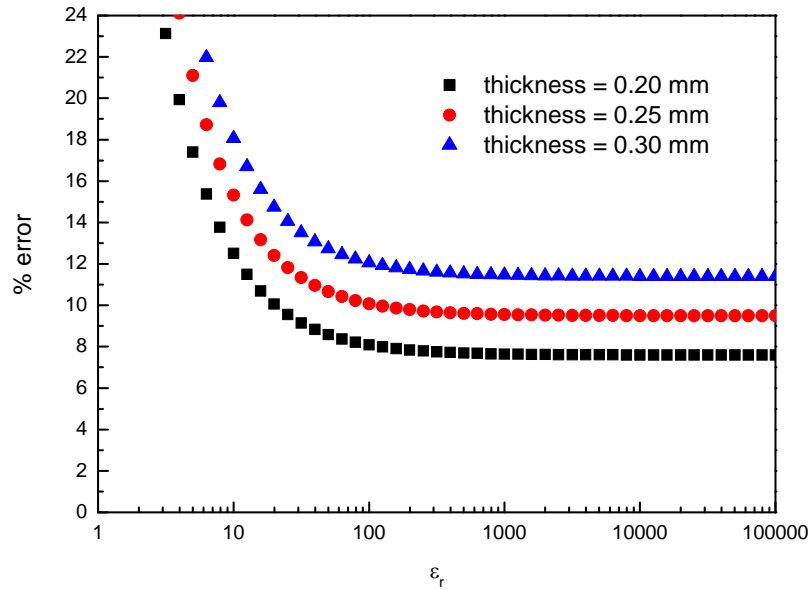
Figure 4.5   Variations of % error with ε_r for the samples with the same partial electrodes (2 mm in diameter) but different thickness.

By using Equations 4.1 – 4.4, the ε_r for the CBT-Cu/Ba-0.30 and MBT-Cu/Ba-0.40, in the form of ceramic disk and double-layered resonator, has been calculated and listed in Table 4.2. It can be seen that for each composition, the calculated ε_r for the sample of different formats are similar. This suggests that the properties of the double-layered resonators are good for the resonator applications.

Table 4.2   Relative permittivity ε_r of the two compositions in different forms: ceramic disk and "double-layered resonators". The relative permittivity is calculated using Equations 4.1 – 4.4, with considering the leakage of electric field at the edges.

	Ceramic disk (full electrode)	Double-layered resonator (3 mm electrode)	Double-layered resonator (2 mm electrode)
CBT-Cu/Ba-0.30	140	148	154
MBT-Cu/Ba-0.40	161	161	164

4.3   Resonance Responses of CBT-Cu/Ba-0.3 Double-Layered Resonators

For comparison, single-plate resonators have also been fabricated following the same procedures, except without the inner electrode, for the double-layered resonators. Both the single-plate and double-layered resonators are of similar thickness (0.23 mm). As the single-plate resonator does not have the inner electrode, it will resonate at the TE1 mode (fundamental thickness extension mode), while the double-layered resonators, because of the inner electrode and the electrical connection, will resonate at the TE2 mode (second harmonic of the thickness extension mode).

Figures 4.6 shows the impedance and phase angle spectra near the TE1 mode resonance for the CBT-Cu/Ba-0.30 single-plate resonators with 2-mm and 3-mm electrodes (in diameter), while those near the TE2 mode for the double-layered resonators are shown in Figure 4.7. As shown in Figure 4.6, there are a lot spurious

modes around the (largest) resonance peak associated with the TE1 mode. This should be partly due to the ineffective trapping of the vibrations in the electroded region. The vibrations leaked from the electroded region propagate in the unelectroded region and are reflected from the edge of the sample. Standing waves at certain frequencies are then formed, thus leading to the spurious vibration modes. It can also been seen that there are more spurious modes in the resonator with 3-mm electrode. As the dimensions of the resonator are the same for both resonators (~ 4.6 × 5.4 mm), the unelectroded region of the resonator with 3-mm electrode is narrower, and hence it is easier for the leaked vibrations to be reflected and then forming the standing waves.

It should be noted that the two relatively large spurious modes, e.g. the ones at ~9.75 MHz and 9.95 MHz for the resonator with 2-mm electrode (Figure 4.6a), are the anharmonic overtone modes. The one closer to the TE2 mode is the first-order asymmetric anharmonic overtone mode A_o, while the other is the second-order symmetric anharmonic overtones mode S_1 [48]. A_o mode is generated by the slight deviation of the electrode positions from the precise one, and is difficult to be removed completely. However, probably because of the larger area, the misalignment between the electrodes becomes less for the resonator with 3-mm electrode and hence the observed A_o mode becomes weaker (Figure 4.6b). S_1 mode can be shifted away from the main mode by decreasing the electrode diameter. Accordingly the observed S_1 mode for the resonator with 2-mm electrode is farer away from the TE2 mode as compared to the resonator with 3-mm electrode. On the other hand, as the impedance is inversely proportion to the (electrode) area, the impedance of the resonator with 3-mm electrode, in particular for the impedance at

resonance frequency Z_{min}, is smaller than that of the resonator with 2-mm electrode.

As shown in Figure 4.7, most of the spurious modes in the double-layered resonators are suppressed. This indicates that the vibrations have been effectively trapped in the electrode region. This should be partly due to the higher trapping efficiency at high frequencies, and partly due to the mode of the TE2 vibrations. Similar results for the anharmonic overtone modes are observed; i.e. the A_o mode becomes weaker and the S_1 mode becomes closer to the TE2 mode as the electrode area increases. As both the A_o and S_1 modes are beyond the TE2 mode (i.e. the corresponding resonance frequencies are out the range between the resonance and anti-resonance frequencies), they do not have a significant influence on the resonator performance [48]. It is also seen that the observed Z_{min} for the resonator with 3-mm electrode is smaller than that of the resonator with 2-mm electrode (14 vs 30 Ω). In fact, the observed Z_{min} for both the resonators are quite small. Z_{min} is one of the most important parameters for resonators. It should be small enough to reduce the energy loss during the operation. For a commercially available PZT resonator with similar resonance frequency, Zmin is about 10 Ω. On the basis of the above results, it can conclude that the CBT-Cu/Ba-0.30 lead-free double-layered resonators have good potential to replace the lead-based resonators.

(a)
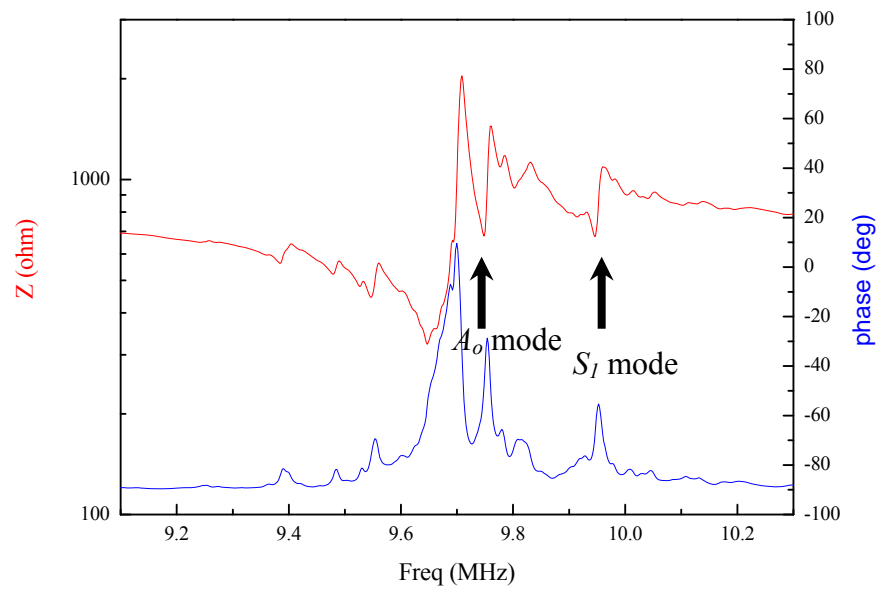
(b)

Figure 4.6   Impedance and phase spectra of the CBT-Cu/Ba-0.30 single-plate resonators with (a) 2-mm electrode and (b) 3-mm electrode.

(a)

(b)

Figure 4.7   Impedance and phase spectra of the CBT-Cu/Ba-0.30 double-layered

resonators with (a) 2-mm electrode and (b) 3-mm electrode.

4.4 Resonance Responses of MBT-Cu/Ba-0.4 Double-Layered Resonators

Figures 4.8 shows the impedance and phase angle spectra near the TE2 mode resonance for the MBT-Cu/Ba-0.40 double-layered resonators with 2-mm and 3-mm electrodes (in diameter). The thickness of the resonators is about 0.27 mm. Similar to CBT-Cu/Ba-0.30, most of the spurious modes in the double-layered resonators are suppressed, indicating that the vibrations have been effectively trapped in the electrode region. Because of the better piezoelectric properties (larger d_{33}), the observed Z_{min} for the MBT-Cu/Ba-0.40 double-layered resonators are smaller than those for the CBT-Cu/Ba-0.30 resonators (15 vs 30 Ω for 2-mm electrode, 16 vs 14 Ω for 3-mm electrode). However, their spectra are not as "clean" as those for the CBT/Cu/Ba-0.30 double-layered resonators. In particular for the MBT-Cu/Ba-0.40 double-layered resonator with 3-mm electrode. This would affect the performance of the resonator and hence is not preferred.
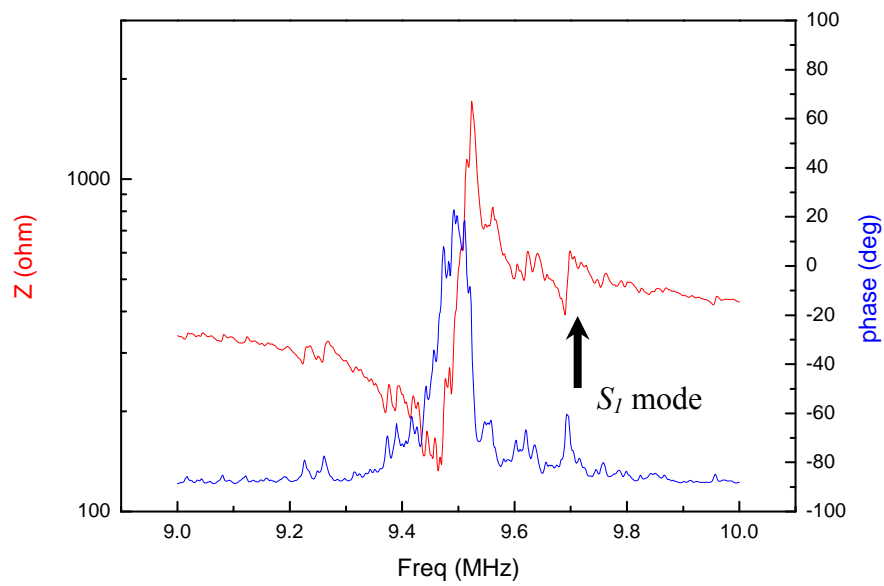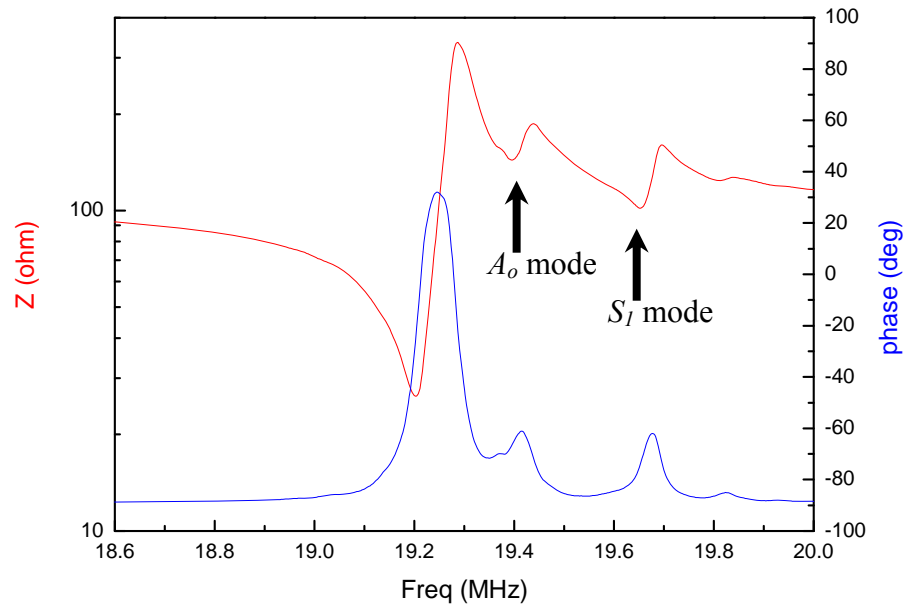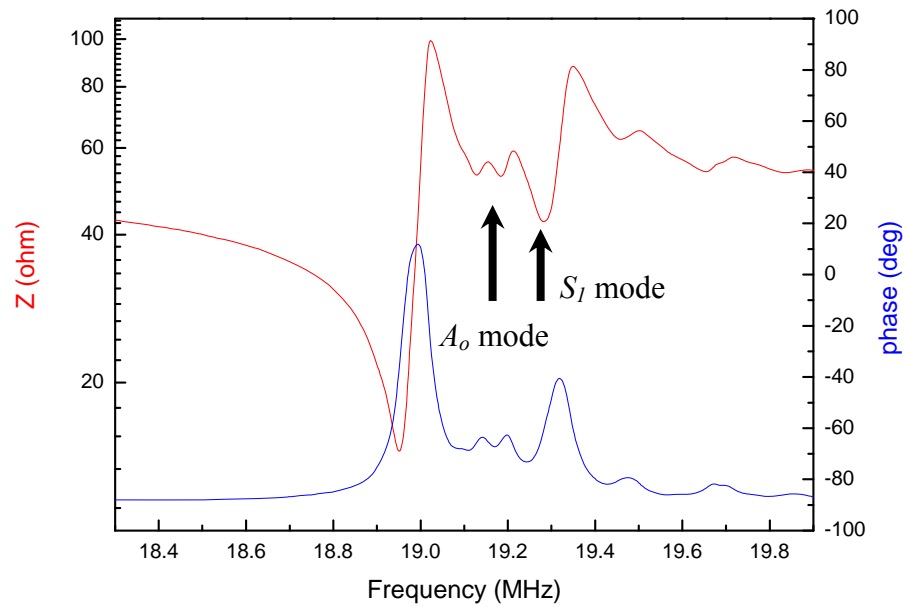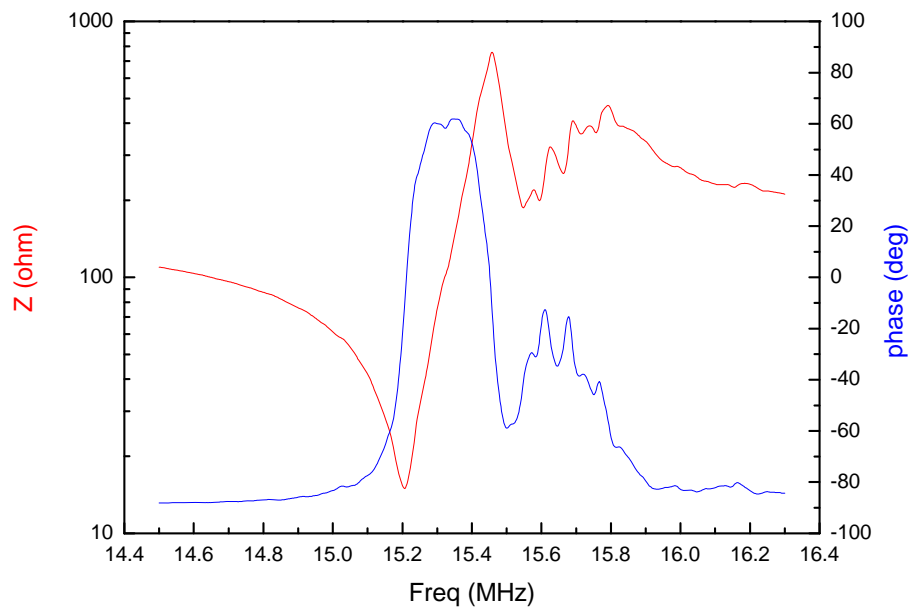
(a)

(b)
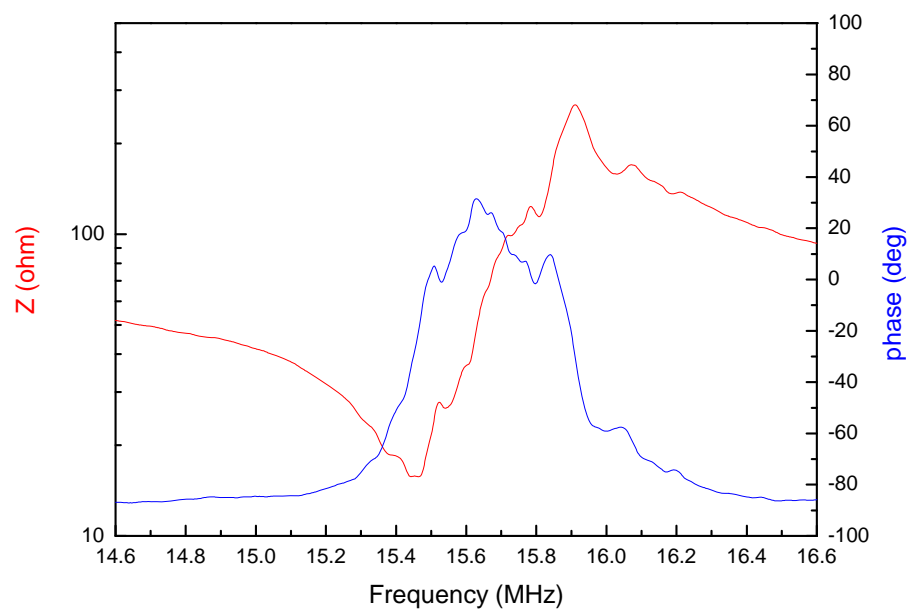
Figure 4.8   Impedance and phase spectra of the MBT-Cu/Ba-0.40 double-layered resonators with (a) 2-mm electrode and (b) 3-mm electrode.

4.5 Temperature Dependence of Resonance Frequency

The thermal stability of a resonator is quantified by the temperature coefficient of frequency *TCF* which is define as

$$TCF = \frac{f_{r-100} - f_{r-30}}{f_{r-30} \times 70} \qquad (4.5)$$

where f_{r-30} and f_{r-100} are the resonance frequencies at 30°C and 100°C, respectively. Figure 4.9 shows schematically the experimental setup for the measurement of *TCF*. The sample was heated in an oven and the resonance response of the sample was measured using an impedance analyzer, from which the resonance frequency was determined.
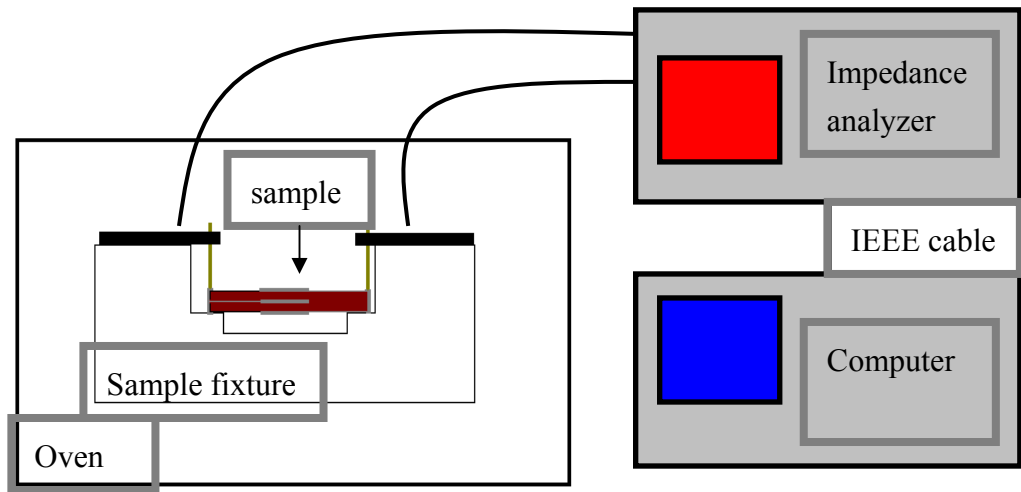
Figure 4.9   Experimental setup for the *TCF* measurement.

The variations of the resonance frequency f_r with temperature for the CBT-Cu/Ba-0.30 and MBT-Cu/Ba-0.40 double-layered resonators are shown in

Figure 4.10 and Figure 4.11, respectively. Using Equation 4.5, the *TCF* for the resonators are determined as -39.3 and -43.2 ppm/^{o}C, respectively. The origin of frequency shifting with temperature may be due to the thermal expansion of the materials. When the temperature increases, the thickness of the resonator increases, and hence f_r decreases, giving a negative *TCF*.
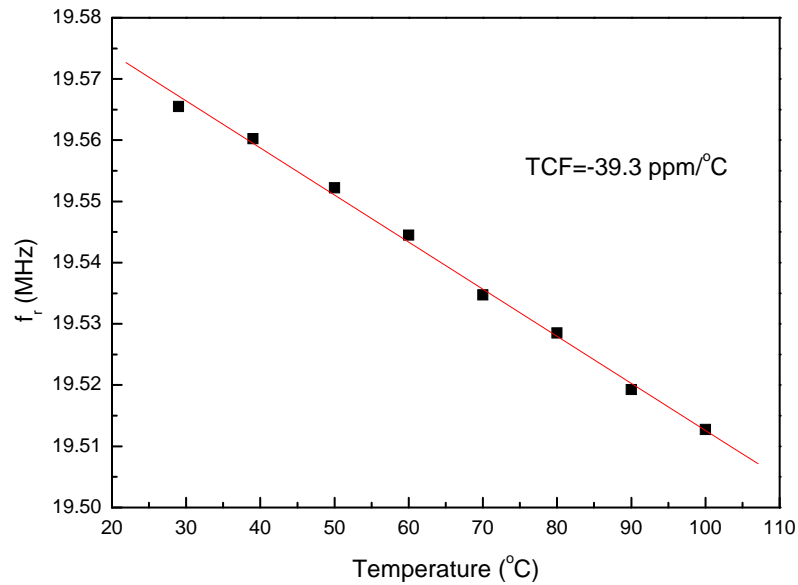
Figure 4.10   Variation of the resonance frequency f_r with temperature for the

CBT-Cu/Ba-0.30 double-layered resonator.
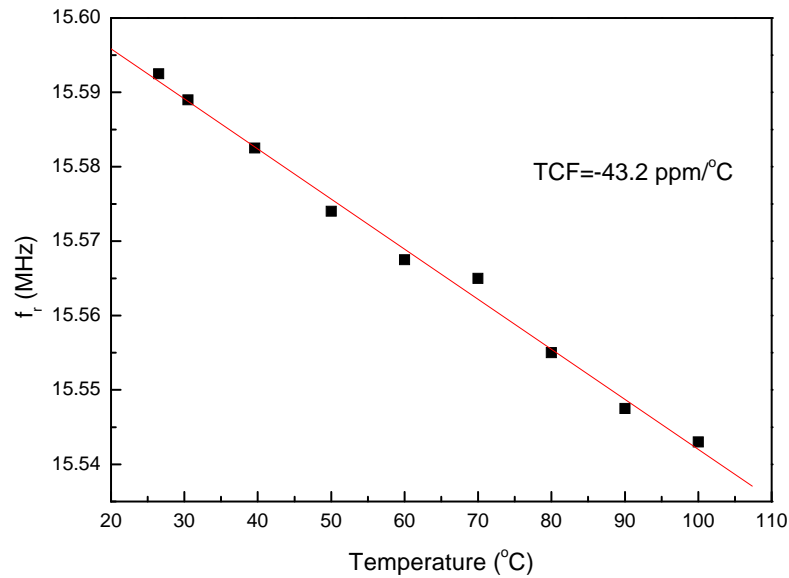
Figure 4.11   Variation of the resonance frequency f_r with temperature for the

MBT-Cu/Ba-0.40 double-layered resonator.

The physical properties and performances of the CBT-Cu/Ba-0.30 and MBT-Cu/Ba-0.40 double-layered resonators are summarized in Table 4.3. As a resonator, there should be no spurious vibration around the main resonant mode and the resonant impedance should be low. Although the MBT-Cu/Ba-0.40 ceramic has better piezoelectric properties, its performance as a resonator is not as good as the CBT-Cu/Ba-0.30. For the CBT-Cu/Ba-0.30 double-layered resonator, it has a relatively "clean" resonance response around the TE2 mode and a lower TCF. Moreover, its Z_{min} is relatively low, and very close to the value for a commercially available PZT resonator. These suggest that the CBT-Cu/Ba-0.30 lead-free double-layered resonators have good potential to replace the lead-based resonators.

Table 4.3   Physical properties and performances of the CBT-Cu/Ba-0.30 and

MBT-Cu/Ba-0.40 double-layered resonators.

	CBT-Cu/Ba-0.30		MBT-Cu/Ba-0.40	
Electrode diameter (mm)	3	2	3	2
Z_{min} (Ω) (TE2 mode)	14	30	16	15
N_{TE2} (Hz·m)	4365	4336	4035	4138
ε_r	152	161	167	172
$tan\,\delta$ (%)	0.45		0.40	
d_{33} (pC/N)	11.1		25.7	
TCF (ppm/^{o}C)	-39.3		-43.2	

Chapter Five

Conclusions

The main objective of the present project is to develop lead-free piezoelectric ceramic resonators for high-frequency oscillator applications (~ 20 MHz). Because of the relatively good ferroelectric properties, $CaBi_4Ti_4O_{15}$ (CBT) and CeO_2-modified $[(Na_{0.5}K_{0.5})_{0.94}Li_{0.06}]_{0.5}Bi_{4.5}Ti_4O_{15}$ (MBT) have been selected as the base materials in this study. The physical properties of the CBT and MBT ceramics have been further improved by doping copper oxide (CuO) and a Cu/Ba complex (in a molar ratio of 71.5/28.5). The ceramics have been successfully fabricated by a conventional mixed-oxide method. Their dielectric, piezoelectric and ferroelectric properties have been investigated in detail. The ceramics with the optimum properties has been used to fabricate resonators and their performances have been evaluated in detail.

Our results reveal that the doping of CuO is effective in improving the densification, enhancing the piezoelectric properties and reducing the dielectric loss of the CBT ceramics. For the CBT-Cu-0.03 (i.e. added with 0.03 wt% CuO) ceramic, its properties become optimum, having a high density (ρ = 6942 kg/m^3), a low dielectric loss ($tan\delta$ = 0.12 %), a large piezoelectric coefficient (d_{33} = 12.4 pC/N), a large planar-mode electromechanical coupling coefficient (k_p = 5.1 %), a high mechanical quality factor (Q_m = 7366), and a high resistivity (ρ_r = 2.5×10^{13} Ω·cm).

The Cu/Ba complex is effective in decreasing the sintering temperature of the CBT and MBT ceramics. The Cu/Ba complex becomes molten at a eutectic temperature of 890°C. As a result, because of the liquid-phase which promoting the densification, the ceramics can be well-sintered at a lower temperature. For the CBT ceramic added with 0.30 wt% of the Cu/Ba complex (i.e. CBT-Cu/Ba-0.30), the sintering temperature is decreased to 990°C, while the other physical properties are either remained almost unchanged or even improved slightly. In summary, it has a high ρ (6756 kg/m^3), a large d_{33} (11.6 pC/N), a large k_p (3.6 %) and a high ρ_r (2.4×10^{13} Ω·cm). As the CBT-Cu/Ba-0.30 ceramic can be well-sintered at a temperature below 1000°C, it has been selected for the fabrication of the double-layered resonators, in which Ag70/Pd30 inner electrodes, instead of Pt inner electrodes, can be used.

For MBT, 0.4 wt% of the Cu/Ba complex is required to decrease the sintering temperature below 1000°C. Unlike CBT, there is degradation in the piezoelectric and dielectric properties of the ceramics even at low addition levels. Nevertheless, the CBT-Cu/Ba-0.40 ceramic (i.e. added with 0.40 wt% of the Cu/Ba complex) has been selected for the fabrication of the double-layered resonators because of its good piezoelectric properties. In summary, it has a large d_{33} (24.5 pC/N), a high ρ (6980 kg/m^3) and a high ρ_r (2.9×10^{13} Ω·cm).

Double-layered resonators with an inner electrode using CBT-Cu/Ba-0.30 and MBT-Cu/Ba-0.4 ceramics have been successfully fabricated by the multilayer techniques, which include roll-casting, screen-printing, stacking and cofiring. As the sintering temperatures of the ceramics are below 1000°C, Ag70/Pd30 inner

electrode, instead of Pt inner electrode, can be used for cofiring with the green samples. The dimensions of the double-layered resonators are about 5.4 mm × 4.5 mm × 0.2 mm, and the resonance frequency is about 19 MHz. The energy trapping technique has been successfully applied by using partial electrodes (electrodes with 2 mm and 3 mm diameters) to suppress the spurious vibrations. In addition, because of the inner electrode, the resonator resonates at the TE2 mode (second harmonic of the thickness extension mode), which is also essential in suppressing the spurious vibrations. Our results also reveal that although the MBT-Cu/Ba-0.40 ceramic has better piezoelectric properties, its performance as a resonator is not as good as CBT-Cu/Ba-0.30. For the CBT-Cu/Ba-0.30 double-layered resonator, it has a relatively "clean" resonance response around the TE2 mode and a lower temperature coefficient of frequency (*TCF* =-39.3 ppm/°C). It also has a relatively low impedance at resonance (14 and 30 Ω for 3-mm and 2-mm electrodes, respectively), which is very close to the value for a commercially available PZT resonator. These suggest that the CBT-Cu/Ba-0.30 lead-free double-layered resonators have good potential to replace the lead-based resonators.

References

[1]   Doerner, S. Universal Impedance Spectrum Analyzer for Sensor Applications. *PROCEEDINGS OF THE IEEE SENSORS*, Vols 1 and 2, 596-599 (2003)

[2]   Murata Manufacturing Co. Ltd. Ceramic Resonators (CERALOCK®) Applications Manual. *CATALOG P17E-14, KYOTO, JAPAN* (2004)

[3]   Jaffe, B. Piezoelectric Ceramics, *ACADEMIC PRESS LTD*. (1971)

[4]   Hom, C. L. Calculation of Quasi-Static Electromechanical Coupling Coefficients for Electrostrictive Ceramic Materials. *I.E.E.E. TRANSACTION ON ULTRASONIC, FERROELECTRICITY AND FREQUENCY CONTROL*, 1994, 41(4), 542

[5]   Z, Lazarevic. An Approach to Analyzing Synthesis, Structure and Properties of Bismuth Titanate Ceramics. *SCIENCE OF SINTERING*, 37 (2005) 199-216

[6]   Mitsui, T. An Introduction To The Physics of Ferroelectrics. *LONDON, GORDON AND BREACH SCIENCE PUBLISHERS LTD.* (1976)

[7]   ANSI/IEEE Std 100-1984, *IEEE STANDARD DICTIONARY OF ELECTRICAL AND ELECTRONICS TERMS* (1984)

[8] Salt, D. Hy-Q handbook of quartz crystal devices. *VAN NOSTRAND REINHOLD, WOKINGHAM* (1987)

[9] A. Ando, *JAPAN PATENT APPLICATION* 1987168491 (1987), equivalent to US patent 4900970

[10] A. Ando, *JAPAN PATENT APPLICATION* 198723548 (1987), equivalent to US patent 4918350

[11] A. Fouskova, *JOURNAL OF APPLIED PHYSICS*, 41 (1970) 2834

[12] S. Ikegami, *JAPANESE JOURNAL OF APPLIED PHYSICS*, 13 (1974) 1572

[13] T. Takenaka, Dr. Thesis, Faculty of Engineering, University of Kyoto, 1985

[14] E. C. Subbarao, A Family of Ferroelectric Bismuth Compounds, *JOURNAL OF PHYSICS AND CHEMISTRY OF SOLID* 23 (1962) 665

[15] I. G. Ismailzade, *SOVIET PHYSICS CRYSTALLOGRAPHY* 12 (1968) 625

[16] Lin Sun. Piezoelectric and Ferroelectric Properties of $SrBi_2(Nb_{1-x}Ta_x)_2O_9$ Ceramics. *MATERIALS SCIENCE AND ENGINEERING B* 135 (2006) 60-64

[17] H. Nagata. Bismuth Layer-structured Ferroelectric $(Sr,Ca)_2Bi_4Ti_5O_{18}$ Ceramics for Lead-free Piezoelectric Resonator Applications. *ULTRASONIC*

SYMPOSIUM, 2005 IEEE, Volume 2, 1077- 1082

[18] Akira, A. Layered Piezoelectric Ceramics for Fine-Tolerance Resonator Applications. *INTERNATIONAL JOURNAL OF APPLIED CERAMIC TECHNOLOGY,* 2[1], 33-44 (2005)

[19] Mortley, W. S. A Waveguide Theory of Piezoelectric Resonance. *MARCONIC REVIEW*, Vol. RD756 (1946)

[20] Shockley, W.. Energy-trapping and Related Studies of Multiple Electrode Filter Crystals. *PROCEEDINGS OF 17TH ANNUAL FREQUENCY CONTROL SYMPOSIUM*, pp. 88-126 (1963)

[21] Shockley, W.. Trapped-energy Modes in Quartz Filter Crystals. *THE JOURNAL OF THE ACOUSTICAL SOCIETY OF AMERICA*, Vol. 41, No. 4, Part 2, pp. 981-993 (1967)

[22] Guttwein, G. K.. Status of Quartz Crystal Research and Development. *PROCEEDINGS OF 17TH ANNUAL FREQUENCY CONTROL SYMPOSIUM*, pp. 190-214 (1963)

[23] Aurivullius, B. Mixed bismuth oxides with layer lattices. II. Structure of Bi4Ti3O12. *ARKIV FUR KEMI*, 1949, 1, 499.

[24] Masaru Miyayama. Function Design of Bismuth Layer-Structured Ferroelectrocs. *JOURNAL OF THE CERAMIC SOCIETY OF JAPAN*, 114 [7] 583-589 (2006)

[25] Haixue Yan. Influence of Sintering Temperature on the Properties of High T_c Bismuth Layer Structure Ceramics. *MATERIALS SCIENCE AND ENGINEERING* B88 (2002) 62-67

[26] Tadashi Takenaka. Current Status and Prospects of Lead-free Piezoelectric Ceramics. *JOURNAL OF THE EUROPEAN CERAMIC SOCIETY* 25 (2005) 2693-2700

[27] Chun-Ming Wang. High Performance Aurivillius Phase Solution-Potassium Bismuth Titanate Lead-free Piezoelectric ceramics with Lithium and Cerium Modification. *APPLIED PHYSICS LETTERS* 89, 202905 (2006)

[28] Haixue Yan. Effects of A-Site (NaCe) Substitution with Na-Deficiency on Structures and Properties of $CaBi_4Ti_4O_{15}$-Based High-Curie-Temperature Ceramics. *JAPANESE JOURNAL OF APPLIED PHYSICS* Vol. 40 (2001) pp. 6501-6505

[29] Tadashi Takenaka. Grain Orientation and Electrical Properties of Some Bismuth Layer-Structured Ferroelectrics for Lead-free Piezoelectric Applications. *FERROELECTRICS*, 336:119-136, 2006

[30] Yuji Noguchi. Ferroelectric Properties of Intergrowth $Bi_4Ti_3O_{12}$-$SrBi_4Ti_4O_{15}$ Ceramics. *APPLIED PHYSICS LETTERS*, Volume 77, Number 22 (2000)

[31] Sung-lak Ahn. Structure and Electrical Characterization of $Bi_5Ti_3Fe_{1-x}Mn_xO_{15}$ System. *MATERIALS RESEARCH BULLETIN* 35 (2000) 825-834

[32] Chang Won Ahn. Dielectric and Piezoelectric Properties of Lead-free $Na_{0.5}Bi_{4.5-x}La_xTi_4O_{15}$ and $Na_{0.5}Bi_{4.5-x}Nd_xTi_4O_{15}$ Ceramics. *FERROELECTRICS* (2002), Volume 273, pp. 261-266

[33] Haixue Yan. A-Site (MCe) Substitution Effects on the Structures and Properties of $CaBi_4Ti_4O_{15}$ Ceramics. *JAPANESE JOURNAL OF APPLIED PHYSICS* Vol. 39 (2000) pp. 6339-6342

[34] Haixue Yan. The Effect of (Li,Ce) and (K,Ce) Doping in Aurivillius Phase material $CaBi_4Ti_4O_{15}$. *MATERIAL RESEARCH BULLETIN* 39 (2004) 1237-1246

[35] Jiangtao Zeng. Ferroelectric and Piezoelectric Properties of vanadium-doped $CaBi_4Ti_4O_{15}$ Ceramics. *MATERIAL SCIENCE AND ENGINEERING* B 117 (2005) 241-245

[36] Liaoying Zheng. The Structure and Piezoelectric Properties of $(Ca_{1-x}Sr_x)Bi_4Ti_4O_{15}$ Ceramics. *MATERIAL SCIENCE AND ENGINEERING* B 99 (2003) 363-365

[37] Jiangtao Zeng. Electrical Properties of Neodymium Doped $CaBi_4Ti_4O_{15}$ Ceramics. *SOLID STATE COMMUNICATIONS* 133 (2005) 553-557

[38] Shujun Zhang. High Temperature Properties of manganese Modified $CaBi_4Ti_4O_{15}$ Ferroelectric Ceramics. *SOLID STATE COMMUNICATIONS* 140 (2006) 154-158

[39] Gurong Li. Microstructure and Ferroelectric Properties of MnO_2-doped Bismuth-layer $(Ca,Sr)Bi_4Ti_4O_{15}$ Ceramics, *JOURNAL OF APPLIED PHYSICS* 98, 064108, (2005)

[40] Chun-Ming Wang. Enhancement of Dielectric and Piezoelectric Properties of $M_{0.5}Bi_{4.5}Ti_4O_{15}$ (M=Na, K, Li) Ceramics by Ce Doping. *SCRIPTA MATERIALIA* 57 (2007) 789-792

[41] Callister, W. D. Materials Science and Engineering: An Introduction. *NEW YORK, JOHN WILEY & SONS*, INC.1997.

[42] Sawyer, C. B. and Tower, C. H. Rochelle Salt as a Dielectric. *PHYSICAL REVIEW 35 (1930) 269*

[43] Ikeda, T. Fundamentals of piezoelectricity. *OXFORD UNIVERSITY PRESS, NEW YORK*, (1990)

[44] Damjanovic, D. Ferroelectric, Dielectric and Piezoelectric Properties of Ferroelectric Thin Films and Ceramics. *REPORT ON PROGRESS IN PHYSICS*, Vol. 61, pp.1267-1324 (1998)

[45] Kwok, K.W. Piezoelectric Ceramic/Piezoelectric Polymer Composites for Ultrasonic Applications, Ph.D. Thesis. *THE HONG KONG POLYTECHNIC UNIVERSITY*, 1997

[46] Wei Zhang. Phase Diagram of the BaO-CuO Binary System. *JOURNAL OF AMERICAN CERAMIC SOCIETY*, 73 [7] 1958-64, 1990

[47] Standard Test Methods for AC Loss Characteristics and Permittivity (Dielectric Constant) of Solid Electrical Insulation. *ASTM-D-150-98 (2004)*

[48] Akira, A. Piezoelectric Resonance Characteristics of $SrBi_2Nb_2O_9$-based Ceramics. *JAPANESE JOURNAL OF APPLIED PHYSICS* Vol. 42 (2003) pp.150-156